Postprint of: Mazur Ł., Koszelow D., Zajusz M., Łapiński M., Bik M., Zając P., Adamczyk A., Rutkowski P., Molin S., Brylewski T., Comparison of Cu1.3Mn1.7O4 spinels doped with Ni or Fe and synthesized via wet chemistry and solid-state reaction methods, designed as potential coating materials for metallic interconnects, JOURNAL OF THE EUROPEAN CERAMIC SOCIETY, Vol. 43, iss. 13 (2023), pp. 5557-5574, DOI: 10.1016/j.jeurceramsoc.2023.05.015

Comparison of $Cu_{1.3}Mn_{1.7}O_4$ spinels doped with Ni or Fe and synthesized via wet chemistry and solid-state reaction methods, designed as potential coating materials for metallic interconnects

[1]Łukasz Mazur, [2]Damian Koszelow, [1]Marek Zajusz, [3]Marcin Łapiński, [1]Maciej Bik, [1]Patryk Zając, [1]Anna Adamczyk, [1]Paweł Rutkowski, [2]Sebastian Molin, [1]Tomasz Brylewski*

[1]AGH University of Science and Technology, Faculty of Materials Science and Ceramics, al. Mickiewicza 30, 30-059 Krakow, Poland

[2]Gdańsk University of Technology, Faculty of Electronics, Telecommunications and Informatics, ul. Narutowicza 11/12, 80-233 Gdańsk, Poland

[3]Gdańsk University of Technology, Faculty of Applied Physics and Mathematics, Institute of Nanotechnology and Materials Engineering, ul. Narutowicza 11/12, 80-233 Gdańsk, Poland

Abstract: The influence of the method applied to synthesize Cu-Mn-O spinel was evaluated. The methods selected for the investigation were EDTA gel processes and solid-state reaction synthesis. From the obtained powders, sinters were prepared and assessed in terms of their properties as potential coating materials. Additionally, the influence of Ni and Fe dopants was evaluated. The results show that the EDTA gel processes method seems to be more suitable for spinel synthesis. This method yields spinels that exhibit electrical conductivity above the required threshold (>50 S/cm) over a temperature range of 400-850°C, and it also ensures continuous spinel matrices and high spinel content. Spinels obtained via solid-state reactions exhibit inferior properties. A higher concentration of Ni allows electrical conductivity to be

*Corresponding author at: AGH University of Science and Technology, Faculty of Materials Science and Ceramics, Al. Mickiewicza 30, 30-059 Krakow, Poland, Tel.: +48 12 617 5229; fax.: +48 12 617 46 41. E-mail address: brylew@agh.edu.pl (T. Brylewski)

improved further, while the opposite tendency is observed for Fe. Finally, it was shown that spinels obtained via EDTA gel processes are promising protective-conducting coating materials for SOEC/SOFCs steel interconnects.

Keywords: protective ceramic coatings, manganese-copper spinel, SOFC/SOEC, electrical properties, interconnects

1. Introduction

Sustainable development, which became a priority for many highly industrialized countries at the turn of the 21st century, will not be possible without solving the issue of energy storage. One of the most promising solutions to this problem entails the use of solid oxide electrolyzer cells (SOECs) to convert excess energy into fuel such as hydrogen via electrolysis. SOECs are constructed by applying the same materials and design solutions used in the case of solid oxide fuel cells (SOFCs) [1–3]. A single cell of these electrochemical devices consists of a cathode, an anode and a solid oxide electrolyte, while the component called the interconnect connects individual cells into stack, allowing the entire device to output a significant amount of power**.** Since the operating conditions specific to SOECs – high operating temperatures (above 650°C), a lifespan of up to 40,000 hours, and exposure to an oxidizing-reducing environment – are very demanding, the criteria set for interconnect materials are very strict. These requirements include high chemical stability, resistance to high-temperature corrosion in both oxidizing and reducing atmospheres, compatibility between the thermal expansion coefficients of interconnect materials and other cell elements as well as low area-specific resistance (ASR), which should not exceed 0.1 $\Omega \cdot cm^2$ at any point during the lifetime of the device [4]. There is currently increased interest in metallic interconnects – particularly those made of heat-resistant ferritic steels.

Ferritic steels have become popular because they are relatively inexpensive to manufacture and easier to machine than their ceramic counterparts, they have a thermal expansion coefficient that closely matches the coefficients of the other electrolyzer components, and they exhibit high thermal and electrical conductivity [5]. The main issue associated with the use of metallic interconnects based on ferritic steel is the increase in ASR that stems from the formation of a Cr_2O_3 scale on the surface of the steel. The scale itself is characterized by low electrical conductivity. In addition, its formation allows chromium to react with oxygen and water vapour, which contributes to chromium evaporation [6]. As a result, a phenomenon known as "electrode poisoning" is observed and the efficiency of the device diminishes [7,8]. In order to mitigate these negative effects, the steel may be coated with protective-conductive layers, many of which are spinel-based [9–11].

The composition of spinel oxides can be expressed by the general formula AB_2O_4. In cubic spinel structures, A and B are metal cations that can occupy tetragonal (A is a divalent ion) or octahedral positions (B is a tri- or quadrivalent ion) [12,13]. Spinel may also form an inverse structure. In such a structure, divalent A cations and half of the trivalent B cations occupy octahedral sites, whereas the rest of the B cations occupy tetrahedral sites. Spinel materials exhibit a wide range of electrical properties; some of them exhibit insulating behavior, while others are metallic conductors. These properties strongly depend on the type of metal ion and its distribution in the unit cell [14,15]. The type of the ions that occupy the octahedral positions determines the electrical properties of the spinel material [14]. Cations with multiple valence states, such as manganese ions, provide the most significant increase in electrical conductivity. Furthermore, reports indicate that electrical conductivity, which is determined predominantly by electron hopping between octahedral sites, can be strongly affected by the preparation method and thermal history of spinels [16,17].

In recent years, coatings based on $Mn_xCo_{3-x}O_4$ (where $0 \leq x \leq 3$) have been intensively studied [12,18]. A widely used practice is to apply dopants (e.g. Cu, Ni, Fe, active elements) to improve the physicochemical properties of coatings [19–24]. Coatings based on a manganese-cobalt spinel are especially popular owing to their unique transport properties. The studies that have been conducted indicate that the use of coatings with a spinel structure in an Mn-Co-O system ensures that the rate of scale growth is reduced and is a strongly limiting factor with regards to chromium evaporation. The possibility of maintaining area-specific resistance at a low level during long-term operation of such layered systems is another important advantage [22,25–27]. However, since cobalt has proven to be carcinogenic, its application requires special safety measures. This is associated with an increase in production costs and a potential health risk for humans. In light of these facts, there is an urgent necessity to eliminate Co from protective-conductive coatings. One interesting alternative is copper. It should be noted that manganese-copper spinels have other potential applications – as spectrally selective solar absorbers [28,29], anodes for lithium-ion battery [30], methanol steam reforming catalysts [31] and electrode materials for supercapacitors [32].

The $Cu_{1.3}Mn_{1.7}O_4$ spinel exhibits significantly higher electrical conductivity (~225 S/cm at 750°C after correcting for porosity) [12] compared to the $MnCo_2O_4$ and $Mn_{1.5}Co_{1.5}O_4$ spinels (~36 S/cm and ~60 S/cm at 800°C, respectively) [33,34] that are currently considered the best coating materials for the surface modification of metallic interconnects applied in SOFCs. Studies on copper-doped spinel in the afore-mentioned Mn-Co-O system demonstrate that this additive also has a beneficial influence on the sinterability of the coating, which is very significant with regard to inhibiting the undesirable chromium evaporation phenomenon [20,35,36]. The noteworthy physicochemical and catalytic properties of Cu-Mn-O spinels stem from the presence of two Jahn-Teller ions – Mn^{3+} and Cu^{2+} – in the material [37]. In the

$MnCo_2O_4$ and $Mn_{1.5}Co_{1.5}O_4$ spinels, the cubic phase is stable within a certain composition range, which also affects their properties. However, the range of composition and temperature in which the cubic phase occurs in the Cu-Mn-O system is far narrower [38]. Cu-Mn-O spinels are also slightly less stable compared to spinels from the Mn-Co-O system due to the higher volatility of copper vapors. It is therefore difficult to obtain a spinel with a nominal composition corresponding to $Cu_{1.3}Mn_{1.7}O_4$. Any deviation from stoichiometry may, however, lead to the formation of additional phases such as CuO or manganese oxides, which will cause electrical properties to grow significantly worse. It is thus very important to apply the most suitable method for the synthesis of the Cu-Mn-O spinel. Numerous synthesis methods have been proposed for this purpose, including Pechini's method [33,39], glycine nitrate process (GNP) [13,40,41], co-precipitation [42] as well as solvothermal [43], hydrothermal [44], and solid-state reactions [45,46]. Wet chemistry methods seems to be particularly effective at obtaining spinel material with high spinel phase content, and the EDTA gel processes method is especially noteworthy [47]. In this case, the use of ethylenediaminetetraacetic (EDTA) acid as a cation-complexing agent allows elements to be distributed more evenly, making it possible to obtain a Cu-Mn-O powder with the intended composition. On the other hand, despite some disadvantages, solid-state reaction methods offer lower energy consumption and simplicity, and they are relatively environment-friendly. These factors are especially important in the context of large-scale industrial production [48].

Like those of manganese-cobalt spinels, the physicochemical properties of Cu-Mn-O spinels can be improved by partial substitution with certain dopants. Ignaczak *et al.* presents the possibility of substituting Cu with Fe in the spinel structure [39] obtained via the Pechini method. According to the authors, in the case of $Mn_{1.7}Cu_{1.3-x}Fe_xO_4$ a small amount of Fe (x = 0.1) does not improve properties considerably. On the other hand, due to the Jahn-Teller distortion of the octahedral sites, a higher concentration of iron (x = 0.3 or 0.5) leads to the

phase transformation into tetragonal spinel. At the same time, a higher amount of the dopant stabilized the spinel phase, as evidenced by the fact that the CuO phase was only present in small amounts or absent altogether. Additionally, while investigating the impact of sintering temperature (900, 1000 or 1100°C) the authors observed that partial substitution of Cu with Fe improved the sinterability of spinels and their thermochemical properties [39]. Bhandage *et al.* investigated the substitution of Cu with Cd in the $Cu_xCd_{1-x}Mn_2O_4$ system [49] obtained via grinding, heating at ~900°C for 100 h, and finally quenching. This study led the authors to the conclusion that below a certain Cu concentration ($x < 0.5$) the spinel undergoes a cubic-to-tetragonal phase transition. Nickel is another that has been studied. Joshi and Petric [50] synthesized Cu-Mn-O spinels doped with Ni using a solid-state reaction method. They then formed them into pellets and sintered them at 1100°C for 72 h. The authors found that Ni can stabilize the cubic phase in a wider temperature region than Fe. In terms of electrical conductivity at 800°C, some improvement was observed when Cu was substituted with Ni, forming $Cu_{0.77}Ni_{0.45}Mn_{1.78}O_4$ (~116 S/cm), when compared to the $Cu_{1.18}Mn_{1.82}O_4$ (~60 S/cm) initial material. Sun *et al.* showed that a Ni-doped $(CuMn)_3O_4$ spinel coating effectively reduced the Cr diffusion rate due to fact that the preference of octahedral sites for Ni^{2+} is higher than for Cr^{3+} ions [51]. Although Ni as a dopant in Cu-Mn-O spinels has been evaluated in some studies on sinters, the information concerning its influence on microstructure is insufficient.

Based on the described observations it can be concluded that the effect of iron or nickel on the physicochemical properties of Cu-Mn-O spinels largely depends not only on the dopant content but also to a large extent on the procedure applied for the synthesis of these ceramic materials. It is therefore worth undertaking further research to establish with high precision the influence that the amount of each dopant has on the structure, microstructure and electrical properties of spinels synthesized via selected wet chemistry methods. This approach can

potentially yield an Mn-Cu-O spinel material with high electrical conductivity, which can subsequently be applied to coat steel substrates with spinels in order to create interconnect materials with superior performance in SOEC/SOFCs applications.

In the presented study, manganese-copper spinel with the starting composition of $Cu_{1.3}Mn_{1.7}O_4$ was synthesized using the EDTA gel processes method and a solid-state reaction applied for reference. Additionally, equal amounts of Cu and Mn in the initial composition were partially substituted with Ni and Fe to evaluate the physicochemical properties of doped Cu-Mn-O spinel and the influence of both synthesis methods on the obtained powders. The properties that are crucial from the point of view of application as coating materials for metallic interconnect were then investigated, including the phase and chemical composition, microstructure, and electrical properties. Finally, as a proof of concept, the selected powder was deposited electrophoretically on a metallic substrate to demonstrate the suitability of the powders obtained via EDTA gel processes as a coating material with protective-conductive properties.

2. Experimental

2.1. Spinel powder synthesis

Spinel powders with the composition of $Cu_{1.3-0.5x}Mn_{1.7-0.5x}M_xO_4$ (where M=Ni or Fe and x=0, 0.1 or 0.3) were obtained using a modified sol-gel method with EDTA as the agent complexing metal cations in an aqueous solution; the applied method is also known as EDTA gel processes. Another batch of samples with the same composition was obtained using a solid-state reaction method.

The starting substrates used for synthesis via EDTA gel processes were manganese(II) nitrate tetrahydrate $Mn(NO_3)_2{\cdot}4H_2O$ (SIGMA-ALDRICH, ≥97.0%), copper(II) nitrate hydrate $Cu(NO_3)_2{\cdot}H_2O$ (SIGMA-ALDRICH, 99.999%), iron(III) nonahydrate $Fe(NO_3)_3{\cdot}9H_2O$

(SIGMA-ALDRICH, 99.999%), nickel(II) hexahydrate $Ni(NO_3)_2 \cdot 6H_2O$ (SIGMA-ALDRICH, ≥97.0%, and ethylenediaminetetraacetic acid ($C_{10}H_{16}N_2O_8$, ALDRICH, 99.995%) – all of analytical-grade purity. Appropriate amounts of each nitrate salt were used to prepare the following nitrate solutions: $Mn(NO_3)_2$, $Cu(NO_3)_2$, $Ni(NO_3)_2$ and $Fe(NO_3)_2$. After the concentrations of these solutions had been determined, they were used to prepare mixtures with the desired Mn:Cu:(Ni,Fe) molar ratio derived from the assumed nominal composition. A 0.1 M EDTA solution was then added to the previously prepared solutions in an amount such that 1 mol of metal cations corresponded to 1.1 mol of the complexing agent. After adding ammonia in an amount required to stabilize the pH level at 8, the solutions were mixed vigorously. The prepared solutions were heated until an amorphous gel had been obtained; this gel was then pyrolyzed for 30 min in air at 500°C, which transformed it into agglomerated powders. These powders were calcinated for 5 h in air at 750°C to obtain fine-grained ones with a specific chemical and phase composition. The powders were then milled in isopropanol for 30 min at 975 rpm in a vibrational-rotational mill with zirconia balls (ball to powder ratio 4:1) and dried for 30 min in a vacuum at 90°C.

For the solid-state reaction method, the following oxides were used as starting substrates: copper oxide, CuO (Chempur, 99%), manganese oxide, MnO (Chempur, 93%), iron oxide, Fe_2O_3 (Chempur, 96%), nickel oxide, NiO (Sigma-Aldrich, 99%). The substrates were weighed in stoichiometric ratios on an analytical balance with an accuracy of four decimal places. To initiate the reaction, the weighed powders were vigorously ground in an agate mortar with ethanol for one hour and then dried for 2 h at 70°C. The next stage involved 5 h of calcination in air at 750°C. Finally, the powders were soaked in isopropanol and underwent 30 min of high-energy grinding in a vibrational-rotational mill with zirconia balls (ball-to-powder ratio 4:1) at 975 rpm. After grinding, the powders were vacuum-dried at 90°C for 30 min.

2.2. Spinel sinter preparation

The appropriate amount of the powder (approx. 400 mg) was formed into green bodies using the biaxial pressing process under the pressure of 50 MPa. The green bodies underwent cold isostatic pressing using a pressure of 250 MPa and were then sintered in air at 1000°C. Both the heating and the cooling rate was 5°C/min, while the dwell time was 2 h. The sintered samples obtained in this way had a diameter of 8 mm and a thickness of 1.2-1.60 mm.

Table 1 lists the sample designations depending on the type and amount of the dopant and the synthesis method. These designations are subsequently used to refer to each sample.

Table 1. Sample designation.

Nominal composition	Sample preparation method	
	EDTA gel processes	Solid state reaction
$Cu_{1.3}Mn_{1.7}O_4$	CuMn-EDTA	CuMn-SSR
$Cu_{1.25}Mn_{1.65}Ni_{0.1}O_4$	CuMnNi0.1-EDTA	CuMnNi0.1-SSR
$Cu_{1.15}Mn_{1.65}Ni_{0.3}O_4$	CuMnNi0.3-EDTA	CuMnNi0.3-SSR
$Cu_{1.25}Mn_{1.65}Fe_{0.1}O_4$	CuMnFe0.1-EDTA	CuMnFe0.1-SSR
$Cu_{1.15}Mn_{1.65}Fe_{0.3}O_4$	CuMnFe0.3-EDTA	CuMnFe0.3-SSR

2.3. Electrophoretic deposition of spinel coating on the metallic substrate

To demonstrate the effectiveness of a powder obtained via EDTA gel processes as a coating material, a coating with the composition $Cu_{1.25}Mn_{1.65}Ni_{0.1}O_4$ was deposited electrophoretically on the Nirosta 4016/1.4016 (Thyssen Krupp VDM GmbH, Germany) ferritic stainless steel. This substrate had the following composition (wt%): Cr-16.2, Mn-0.34, Si-0.35, Ni-0.04, P-0.02 and balance Fe [52]. The solution applied for the electrophoretic deposition consisted of a 75:25 v/v mixture of acetone (Chempur, 99.9%) and ethanol (Chempur, 99.8%) mixed with the synthesized CuMnNi0.1-EDTA powder (concentration of 10 g/dm^3). Iodine at a concentration of 1.5 g/dm^3 (Sigma-Aldrich, ≥99.8%) was introduced into the solution, acting as a dispersant. Before the deposition of the coating, the solution was homogenized for 15 min in an ultrasonic bath. The deposition conditions were as follows:

voltage – 60 V, deposition time – 60 s, distance between electrodes – 10 mm. The coatings were dried for 24 h in air at 70°C. To obtain a coating with the appropriate density, the samples underwent a two-stage thermal treatment; the first stage involved 6 h of reduction in an Ar+10% H_2 gas mixture at 1000°C, while the second stage was 8 h of re-synthesis in air at 850°C. The obtained coating/steel layered system and an unmodified steel sample were oxidized for 2000 h in air at 800°C. The oxidation kinetics of these samples were measured using thermogravimetry – by determining the mass gained after each 100 h interval. At each measurement point, the samples were removed from the furnace, left to cool to ambient temperature, and then weighed with an accuracy of 1.0×10^{-5} g.

2.3. Material characterization

Thermal analysis (DSC/TG) of the precursor gels obtained using EDTA gel processes was carried out using the NETZSCH STA 449 F3 apparatus. The gels were heated in air at a rate of 10°C/min over the temperature range of 25-1000°C.

Additionally, to determine the chemical states of elements in the studied samples, X-ray photoemission spectroscopy (XPS) measurements were performed. XPS analyses were carried out at room temperature under ultra-high vacuum conditions, at pressures below 1.1×10^{-6} Pa, using Omicron NanoScience equipment. The data were analyzed with the CASA XPS software. The Shirley background subtraction and Gauss-Lorentz curve-fitting algorithm applied by means of the GL (30) least-squares method was used for spectra deconvolution. All spectra were calibrated to obtain a binding energy of 285.00 eV for the C 1s line.

The phase composition of the samples was investigated using the X-ray diffraction method (XRD). For this purpose, the Panalytical X'Pert Pro PW 3710 diffractometer was used with CuKα monochromatic radiation. The HighScore Plus compute software and the standard PCPDFWIN v.2.3 data set was used to identify the phase composition of the tested materials.

The mass fractions of individual phases as well as their lattice parameters were determined via Rietveld refinement.

Scanning electron microscopic (SEM) observations of the morphology of the samples were carried out by means of the Phenom XL microscope (Thermo Fisher Scientific) equipped with an integrated X-ray microanalyzer with energy dispersive X-Ray spectroscopic (EDS) capability. The porosity was calculated using dedicated Porometric software (Thermo Fisher), for SEM microscopes which analyzed SEM images. For each sample, we took 25 SEM images (3000× magnification) from different regions. Final porosity was the average of the porosities obtained from each of the 25 analysed images. The program determines the percentage of dark areas (pores) in relation to the entire image and on this basis determines the porosity. Dilatometric tests were carried out using DIL 402C manufactured by Netzsch and equipped with a linear displacement transducer. The tested green bodies were heated in air over a temperature range of 25-1050°C and at a rate of 10°C/min.

The Bruker Vertex 70v spectrometer was used to conduct Fourier transform infrared spectroscopic (FTIR) studies in the mid- (MIR) and far-infrared (FIR) ranges in a vacuum. The transmission technique was used; this involved mixing ca. 2 mg of each well-ground sample with 400 mg of KBr (Uvasol®, Merck) and 180 mg of polyethylene (Uvasol®, Merck) – these two materials are used as reference for the MIR and FIR ranges, respectively – and subsequently pressed with an oil press. 256 and 512 scans at a resolution of 2 cm^{-1} were run within the 4000-400 cm^{-1} (MIR) and 400-100 (FIR) ranges, respectively. The OPUS 7.2. software was used to record spectra and to process the obtained data, which included cropping the MIR spectra to the 800-400 cm^{-1} range due to the absence of significant bands in the remaining sections. The positions of individual bands were estimated with the Peak Picking function.

The electrical conductivity of the studied samples was measured in air using the two-probe four-point DC method, and this was combined with measurements of the Seebeck coefficient over the temperature range of 300-850°C. The custom setup applied for this purpose consisted of a Keysight 33210A generator of function/arbitrary waveform, TF1200 tube furnace, Keysight 34465A multimeter, CFRASB-1000 control unit, SSC-15 measuring probe, BR07 retaining decade and AM16/32B multiplexer. Rectangular-shaped samples were prepared using a machine saw from the sinters and then polished with 2000-grit SiC abrasive paper; their dimensions were measured with a calliper. The thus-prepared samples were heated to 850°C, and then as the samples cooled the electrical resistance was measured at steps of 25°C, down to 300°C. The relative error of the performed electrical conductivity measurements can be estimated to be ~5% of the determined absolute values. Electrical conductivity was calculated based on the following formula:

$$\sigma = \frac{L}{S \cdot R} \tag{1}$$

where: R – sample resistivity [Ω], L – sample thickness [cm], S – area of the Pt electrodes [cm^2]. The obtained electrical conductivity data were adjusted for porosity. For this purpose, the Brueggemann model was applied according to the following formula [53]:

$$\sigma = \sigma_m \cdot \frac{1}{(1-p)^{3/2}} \tag{2}$$

where: σ – conductivity after adjusting for porosity [S/cm], σ_m – measured conductivity [S/cm], p – sinter porosity [-].

The electrical resistance of steel/coating and steel/scale layered systems obtained after oxidation is usually measured in terms of their area-specific resistance (ASR). Due to the symmetrical design of the samples, their ASR was calculated based on the obtained resistance values using the following formula:

$$ASR = \frac{R \cdot A}{2} \quad (3)$$

where: R – electrical resistance [Ω], and A – surface area of the Pt layer [cm^2].

3. Results and discussion

3.1. Characteristics of the gel precursors

The CuMn-EDTA, CuMnNi0.1-EDTA, CuMnNi0.3-EDTA, CuMnFe0.1-EDTA and CuMnFe0.3-EDTA gels obtained after synthesis via EDTA gel processes were thermally evaluated using DSC/TG. This allowed the appropriate conditions for the calcination of gel precursors to be applied, and made it possible to obtain powders with the desired physicochemical properties, including phase and chemical composition and a fine-crystalline structure. The DSC/TG curves shown in Fig.1 were recorded for the studied gels over the range of 25-1000°C.

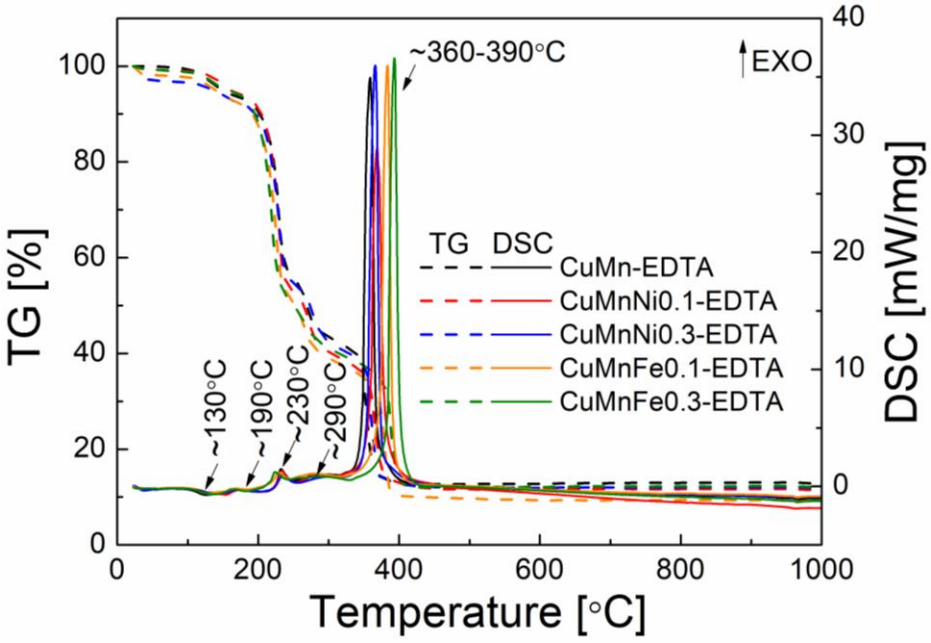

Fig. 1. DSC/TG curves for studied gels obtained via EDTA gel processes.

The shape of the TG curves indicates that the decomposition process consisted of four steps. Additionally, the DSC curves revealed some accompanying exo- and endothermic reactions. The first mass loss in the range of 25-200°C (ca. 6-9% of the initial mass, based on the analyzed sample) can be attributed to the removal of adsorbed and crystallization water, with two associated endothermic effects (at ~130 and ~190°C). The second and third losses of mass – ca. 38-42% and ca. 13% of the initial mass, respectively – were observed in the range of 200-240°C and 240-340°C, respectively. These mass losses were accompanied by two weak exothermal effects (at ~230 and 290°C) and can be attributed to the combustion of metal nitrates used for the synthesis [54].

Finally, in the 350-430°C range the last mass loss (ca. 27-29% of the initial mass) was detected, with a strong accompanying exothermal effect (at ~360-390°C, depending on sample type). This effect was related to the combustion of the organic matrix, which was present in the gels after synthesis.

Overall, the total weight loss during synthesis via EDTA gel processes was ~90 wt%. The presented results suggest that in order for the gels to be calcinated completely, the temperature of at least 600°C is required. However, taking into account the phase diagram of the Cu-Mn-O spinel [38] – particularly with regard to the narrow range over which cubic spinel is stable – as well as the proposed stoichiometry, the optimal temperature for its calcination was determined to be 750°C.

3.2. Chemical and microstructural characterization of powders

After the calcination and the high-energy milling process, the powders obtained using both synthesis methods were evaluated in terms of morphology and chemical composition. Table 2 shows the results of the chemical analysis of the powders in relation to the nominal composition (with an accuracy of ~1-2%).

Table 2. Chemical composition of powders obtained via EDTA gel processes or a solid-state reaction.

Nominal composition	Sample name	Metal ratio				Corresponding spinel composition
		Cu	Mn	Ni	Fe	
$Cu_{1.3}Mn_{1.7}O_4$	CuMn-EDTA	0.44	0.56	-	-	$Cu_{1.32}Mn_{1.68}O_4$
	CuMn-SSR	0.45	0.55	-	-	$Cu_{1.35}Mn_{1.65}O_4$
$Cu_{1.25}Mn_{1.65}Ni_{0.1}O_4$	CuMnNi0.1-EDTA	0.42	0.55	0.03	-	$Cu_{1.26}Mn_{1.65}Ni_{0.09}O_4$
	CuMnNi0.1-SSR	0.43	0.52	0.05	-	$Cu_{1.29}Mn_{1.56}Ni_{0.15}O_4$
$Cu_{1.15}Mn_{1.65}Ni_{0.3}O_4$	CuMnNi0.3-EDTA	0.39	0.51	0.10	-	$Cu_{1.17}Mn_{1.53}Ni_{0.3}O_4$
	CuMnNi0.3-SSR	0.41	0.47	0.12	-	$Cu_{1.23}Mn_{1.41}Ni_{0.36}O_4$
$Cu_{1.25}Mn_{1.65}Fe_{0.1}O_4$	CuMnFe0.1-EDTA	0.43	0.54	-	0.03	$Cu_{1.29}Mn_{1.62}Fe_{0.09}O_4$
	CuMnFe0.1-SSR	0.41	0.55	-	0.04	$Cu_{1.23}Mn_{1.65}Fe_{0.12}O_4$
$Cu_{1.15}Mn_{1.65}Fe_{0.3}O_4$	CuMnFe0.3-EDTA	0.39	0.50	-	0.11	$Cu_{1.17}Mn_{1.50}Fe_{0.33}O_4$
	CuMnFe0.3-SSR	0.41	0.49	-	0.10	$Cu_{1.23}Mn_{1.47}Fe_{0.3}O_4$

The obtained results indicate that EDTA gel processes yield powders with a composition that is closer to the nominal composition than in the case of the solid-state reaction method.

Fig. 2 presents examples of SEM images of CuMn-EDTA and CuMn-SSR powders after calcination and high-energy milling.

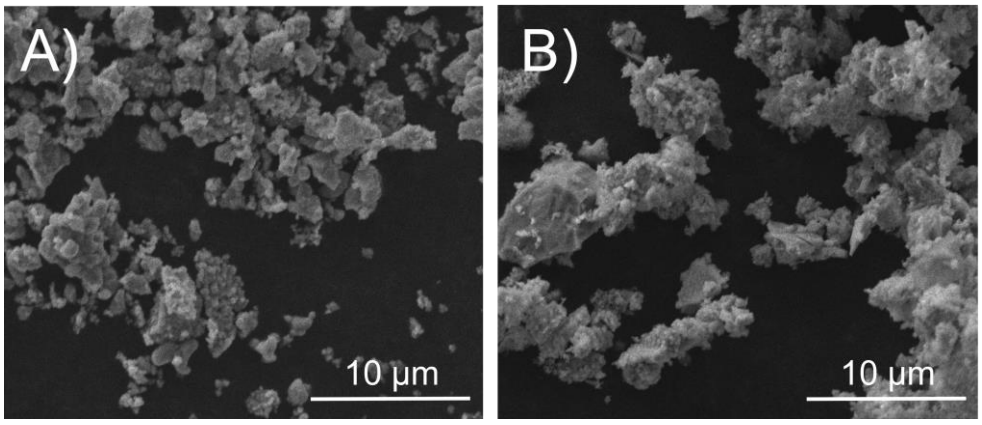

Fig. 2. SEM images of A) CuMn-EDTA and B) CuMn-SSR powders obtained after calcination and high-energy milling.

Some minor differences can be found between the powder prepared using the two synthesis methods. The particle size of the powders obtained via EDTA gel processes was

typically in the ~250-450 nm range, but some larger particles with a size of ~1-1.5 μm were also present. In the powder obtained using the solid-state reaction, the smaller particles were similar in size to those in the CuMn-EDTA powders, but some of the larger ones were as large as ~4-8 μm. No larger particle agglomerations were observed. Nickel and iron dopants did not appear to influence particle morphology.

3.3. Sintering properties of compacted powders

Prior to the physicochemical characterisation of spinel sinters, dilatometric studies were carried out to determine the sintering temperature of the compacted powders obtained via the EDTA gel processes and solid-state reaction methods. Fig. 3 shows the dilatometric curves recorded for the green bodies received after calcinating and milling the powders.

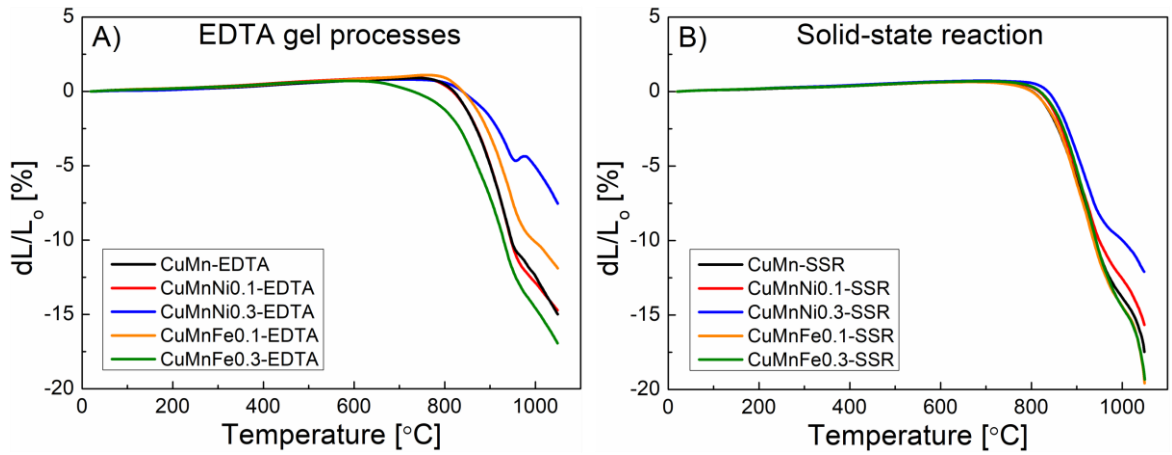

Fig. 3. Dilatometric curves recorded for green bodies obtained via A) EDTA gel processes, and B) solid-state reaction.

As temperature increased, the green bodies expanded by ~1% and then sintering began. Based on Fig. 3A it can be observed that the densification process for all analyzed pellets begins at approximately 675°C for CuMnFe0.3-EDTA and in the range of 725-760°C for the other investigated systems. During the study, the most pronounced shrinkage was observed for the CuMnFe0.3-EDTA sample (~17%), while the lowest one was for CuMnNi0.3-EDTA

(~8%). Moreover, for CuMnNi0.3-EDTA the sinter (~1%) was found to expand near 975°C. This can be attributed to the intensive formation of CuO. For the undoped spinel material (CuMn-EDTA) the shrinkage was about ~15%. On the other hand, by analyzing the dilatometric curves presented in Fig. 3B, it can be concluded that in the case of the samples prepared via the solid-state reaction the densification process for all green bodies began in the range of 680-710°C. The most intensive shrinkage was observed for green bodies of CuMnFe0.1-SSR and CuMnFe0.3-SSR (almost 20%). At the same time, the lowest shrinkage was detected for CuMnNi0.3-SSR (~12.5%), as had been the case with the corresponding powder obtained via the EDTA gel processes. Undoped samples exhibited a shrinkage of ~18%. The conducted dilatometric studies showed that doping with a sufficient amount of iron can enhance the sinterability of spinel powder, while the opposite is true for higher nickel content. It was also observed that the synthesis method can affect the point at which densification process starts and the overall shrinkage of the tested systems. Additionally, due to the investigated material's target application, the degree of densification should be as high as possible. Consequently, a high sintering temperature should be applied; however, the maximum effective sintering temperature determined from the CuO-MnO_2 phase diagram [38] should not exceed approximately ~1000°C. On the other hand, Waluyo *et al.* [33] investigated the sintering behaviour of $Cu_xMn_{3-x}O_4$ green bodies obtained from Pechini-derived powders for x=1-1.5. The authors observed that the maximum shrinkage rate was at temperatures in the 850-910°C range, with the sintering process completed at 1000-1050°C. In the same study, the authors investigated cobalt-based spinel ($Mn_{1.5}Co_{1.5}O_4$) for comparison, and demonstrated that replacing Co with Cu significantly enhanced the sintering characteristics.

It is important to emphasize the fact that the spinel samples obtained from powders prepared via EDTA gel processes were characterized by lower shrinkage than those obtained

from powders prepared using the solid-state reaction method. The spinel coating prepared with the former type of materials may therefore be less prone to cracking during the thermal treatment performed for the purpose of its formation on the metallic substrate.

3.4. Phase composition of the powders and sinters

Fig. 4 shows the diffraction patterns recorded for the powders (Fig. 4A and B) and sinters (Fig. 4C and D) of Cu-Mn-O spinels (with and without the Ni and Fe dopants) for both powder synthesis methods.

Fig. 4A presents the XRD results for the CuMn-EDTA, CuMnNi0.1-EDTA, CuMnNi0.3-EDTA, CuMnFe0.1-EDTA and CuMnFe0.3-EDTA powders. XRD phase analysis revealed that after calcination the powders consisted of two phases – either $Cu_{1.5}Mn_{1.5}O_4$ (undoped sample) or $Cu_{1.4}Mn_{1.6}O_4$ (for all doped samples) spinel with a cubic structure (space group Fd-3 m, ICDD 01-070-0262 and ICDD 01-071-1145 respectively) and a small amount of monoclinic CuO (space group C2/c, ICDD 00-048-1548). The presence of both phases is in agreement with the Cu-Mn-O phase diagram, from which it follows that higher temperatures may lead to the decomposition of the spinel cubic phase into a cubic one and CuO [38]. The presence of CuO after powder calcination had previously been observed by Bobruk *et al.* [47] and Ignaczak *et al.* [39].

Fig. 4B shows the results of diffraction studies conducted for CuMn-SSR, CuMnNi0.1-SRR, CuMnNi0.3-SSR, CuMnFe0.1-SSR and CuMnFe0.3-SSR spinel powders obtained via solid-state reaction. These powders contained one more phase than those obtained via EDTA gel processes. In addition to the $CuMn_2O_4$ cubic spinel (space group Fd-3m, ICDD 01-073-1605) and the monoclinic CuO (space group C2/c, ICDD 00-048-1548), orthorhombic Mn_2O_3 (space group Pbca, ICDD 01-071-0635 or ICDD 00-024-0508) was also detected. Although bixbyite may be present along with the spinel phase when a low sintering temperature is

applied and the Mn concentration in the spinel is high, in this case the orthorhombic phase was likely a remnant of unreacted Mn_2O_3 powder after the solid-state synthesis.

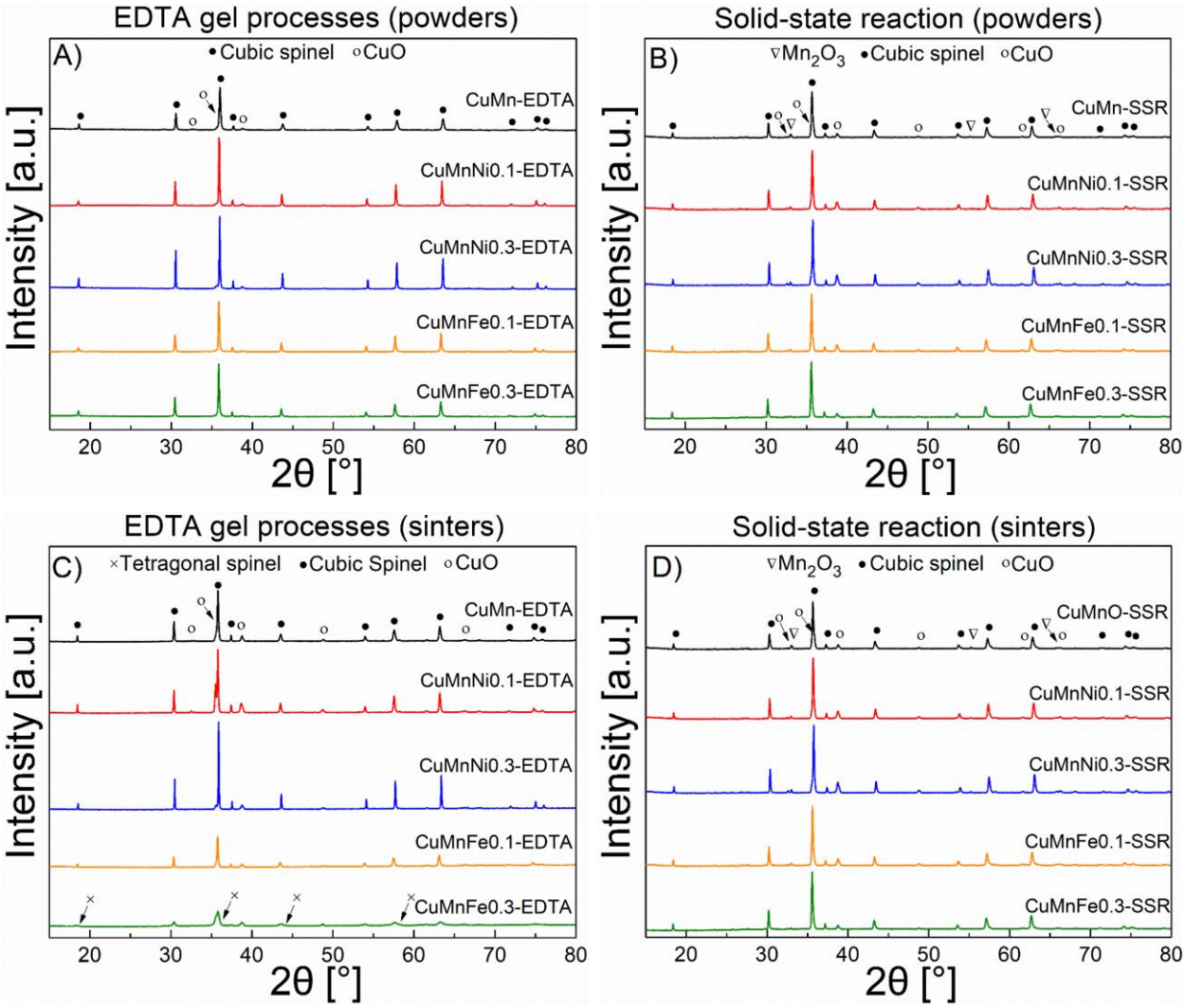

Fig. 4. Diffraction patterns recorded for powders synthesized via A) EDTA gel processes and B) solid-state reaction method, as well as the corresponding sinters: C) and D), respectively.

It should be noted that the spectra recorded for powders obtained via both methods did not indicate the presence of either nickel or iron oxide, which suggests full incorporation into the spinel structure.

Tables 3 and 4 list the lattice parameters of the unit cells of the studied spinel. In general, lattice parameter *a* for the powders obtained via the solid-state reaction tended to be higher than for the corresponding spinel powders obtained via EDTA gel processes.

Table 3. Relative mass fractions of phases identified in the powders obtained via EDTA gel processes and the corresponding sinters.

Sample type	Sample name	Mass fraction [%]			Lattice parameter *a* [Å]
		Spinel	Mn_2O_3	CuO	
Powder	CuMn-EDTA	92.2	-	7.8	8.2861(1)
	CuMnNi0.1-EDTA	94.9	-	5.1	8.2957(1)
	CuMnNi0.3-EDTA	92.1	-	7.9	8.2816(4)
	CuMnFe0.1-EDTA	93.4	-	6.6	8.3011(9)
	CuMnFe0.3-EDTA	96.4	-	3.6	8.3156(3)
Sinter	CuMn-EDTA	84.0	-	16.0	8.3186(4)
	CuMnNi0.1-EDTA	86.5	-	13.4	8.3063(5)
	CuMnNi0.3-EDTA	86.2	-	13.8	8.2984(1)
	CuMnFe0.1-EDTA	84.4	-	15.6	8.3315(3)
	CuMnFe0.3-EDTA	68.2 C*	-	21.9	8.2948(2)
		9.9 T**			*a*=6.0151(8) *c*=8.8374(4)

* – cubic structure, **– tetragonal structure

When considering the influence of the introduced dopants on the unit cell parameter, it can be noticed that for the powder obtained using the solid-state reaction method, the addition of nickel results in the compression of the unit cell, while iron causes its expansion. A similar effect was observed for the powders obtained via the EDTA gel processes with the exception of the CuMnNi0.1-EDTA powder, for which a small addition of nickel caused the unit cell to expand slightly. For the sinters obtained from both types of powders, compression of the unit cell after the addition of nickel was also observed. The introduction of a larger amount of nickel resulted in a more pronounced compression of the unit cell for both powders and sinters.

Table 4. Relative mass fractions of phases identified in the powders obtained by means of the solid-state reaction method and the corresponding sinters.

Sample type	Sample name	Mass fraction [%]			Lattice parameter *a* [Å]
		Spinel	Mn_2O_3	CuO	
Powder	CuMn-SSR	85.5	6.5	8.0	8.3672(2)
	CuMnNi0.1-SSR	77.9	2.5	19.6	8.3490(5)
	CuMnNi0.3-SSR	74.3	3.3	22.4	8.3381(7)
	CuMnFe0.1-SSR	78.8	3.5	17.7	8.3715(5)
	CuMnFe0.3-SSR	90.9	3.5	5.6	8.3779(5)
Sinter	CuMn-SSR	86.0	5.9	8.1	8.3671(9)
	CuMnNi0.1-SSR	77.4	2.9	19.7	8.3571(4)
	CuMnNi0.3-SSR	75.3	2.5	22.1	8.3298(8)
	CuMnFe0.1-SSR	79.2	3.5	17.3	8.3716(1)
	CuMnFe0.3-SSR	88.0	1.7	10.3	8.3852(1)

Fig. 4C presents the diffraction patterns recorded for the sinters prepared from the powders obtained via EDTA gel processes. Phase analysis revealed that these sinters generally consisted of two phases, as did the initial powders. These phases were the $CuMn_2O_4$ spinel with a cubic structure (space group Fd-3m, ICDD 01-084-0543) and monoclinic CuO (space group C2/c, ICDD 00-048-1548). However, in the case of CuMnFe0.3-EDTA, the XRD results also indicated the presence of tetragonal $CuMn_2O_4$ spinel (space group I41/amd, ICDD 00-034-1322). The presence of a tetragonal phase after introducing larger amounts of Fe had already been observed [39]. Its formation is explained by the Jahn-Teller effect, i.e. the elongation of the octahedral sites along the *c* axis [55]; in this case this effect is caused by the presence of octahedrally coordinated Mn^{3+} cations (or possibly also Cu^{2+}) [55,56].

Based on Rietveld's quantitative analysis shown in Table 4 it was observed that the content of the spinel phase in the sinters was lower than in the initial powders. This observation can be associated with the high sintering temperature, at which the spinel phase undergoes thermal decomposition into CuO. The CuMnFe0.3-EDTA sinter exhibited lower cubic phase content than the remaining samples; however, the total spinel content, including the tetragonal phase, was at a similar level. Lattice parameter *a* of the spinel was generally

higher for the sinters than for the powders. Additionally, the addition of 0.1Ni lead to a decrease in the sinters' *a* parameter, rather than an increase, as in the case of the powders. The addition of 0.1Fe caused the cubic cell parameters to increase. For CuMnFe0.3-EDTA, parameter *a* of the cubic phase decreased significantly, but this can be attributed to the partial transition into the tetragonal phase.

The XRD results for the sinters prepared from the powders obtained via the solid-state reaction method are presented in Fig. 4D. In this case, phase composition was again similar to the initial powders. Both the sinters and the powders consisted of the same phases, namely the $CuMn_2O_4$ cubic spinel (space group Fd-3m, ICDD 01-073-1605 or ICDD 01-071-1143) or monoclinic CuO (space group C2/c, ICDD 00-048-1548) and the orthorhombic Mn_2O_3 (space group Pbca, ICDD 01-071-0635 or ICDD 00-024-0508). For the CuMnFe0.3-SSR sinter, no tetragonal phase was detected. Lattice parameter *a* of spinel for sinters CuMn-SSR and CuMnFe0.1-SSR was on a similar level or slightly higher in comparison to the corresponding initial powders. The quantitative analysis presented in Table 4 shows that for this method of powder synthesis, the amount of each phase before and after the sintering process is on a relatively constant level. The only noticeable difference in phase composition was observed for CuMnFe0.3-SSR, in which sintering resulted in increased CuO content and a decreased amount of Mn_2O_3.

3.5. IR spectroscopy

IR spectroscopy is a very apt tool for the determination of possible substitutions with Ni and Fe within the proposed $CuMn_2O_4$ spinel structure, as four IR-active bands can be found for type II and type III spinels with a cubic structure according to the group theory – two in the MIR range (ν_1 and ν_2), assigned typically to vibrations of octahedral units, and two in the

FIR range (ν_3 and ν_4), originating mostly from mixed octahedral and tetrahedral units (ν_3) or tetrahedral units alone (ν_4) [57,58].

Fig. 5 demonstrates the combined spectra from the MIR and FIR ranges. Two main MIR regions of absorption were observed at ca. 580 cm^{-1} and 475 cm^{-1} (Fig. 5) – these regions can be attributed to ν_1 (Cu-O with highly likely Cu^{2+} ionization state [59–61] and Mn-O with highly likely Mn^{3+} ionization state [57]) and ν_2 (Mn-O with highly likely Mn^{3+}/ Mn^{4+} ionization state [59–61]) octahedral modes, respectively.

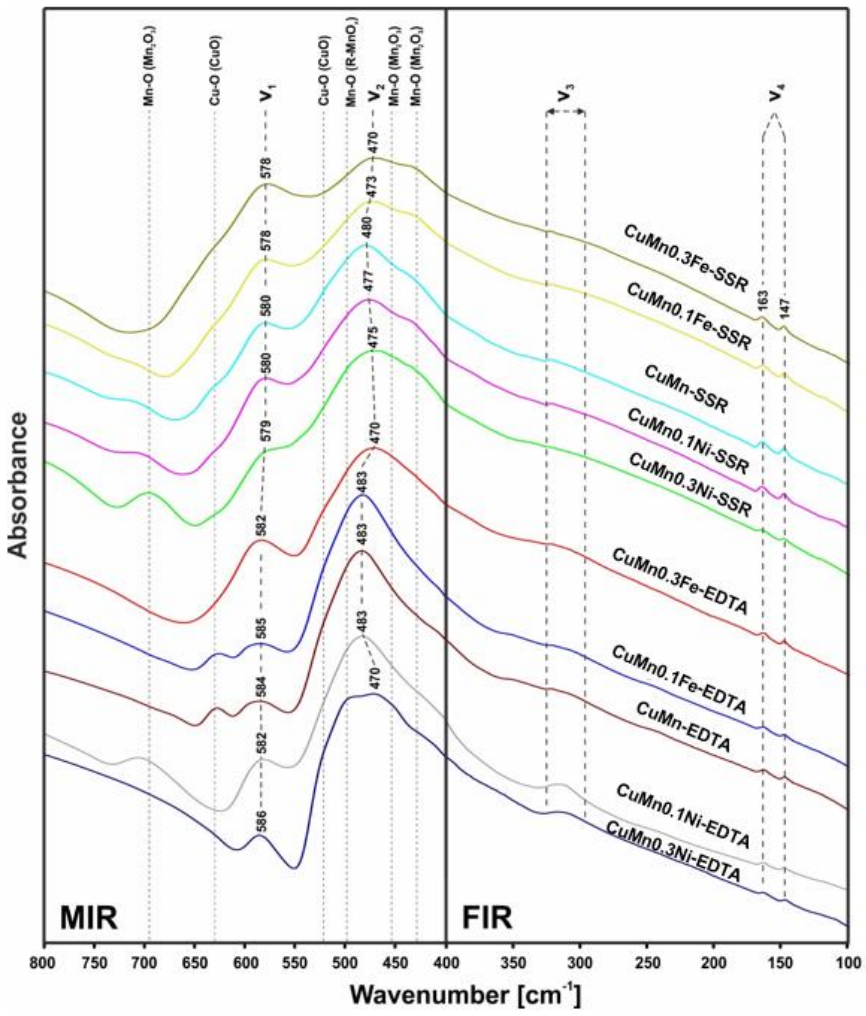

Fig. 5. Mid- (MIR) and far-infrared (FIR) spectra with marked positions of spinel bands ν_1 - ν_4.

The impact of substituting cations on FTIR spectra can be explained with the concept of cation "covalency" proposed in [62]. By calculating the N-V parameter (where N is the number of unpaired electrons and V is the valence state), it is possible to estimate bond strength taking into consideration the fact that valence states can be different for Mn, Cu and Fe. Higher N-V values results in lower covalency (shifting the electron density from oxygen towards metal cations), leading to lower bond strength and, finally, a band shift towards lower wavenumbers in FTIR spectra [16,63]. The N-V parameter of the investigated materials can be calculated as follows: (Cu^{2+}: 1 – 2 = -1), (Mn^{3+}: 4 – 3 = 1), (Mn^{4+}: 3 – 4 = -1), (Ni^{2+}: 2 -2 = 0) and (Fe^{2+}: 5 – 2 = 3).

As no change up to the resolution (2 cm^{-1}) can be considered meaningful, no significant shift of ν_1 band was found. This indicates that the conducted substitution did not affect Cu^{2+} and Mn^{3+} cations. On the other hand, for the ν_2 band, a clear shift towards lower wavenumbers and the broadening of bands can be seen, especially for higher concentrations of dopants. Since Mn^{3+} had likely not been substituted, it is highly probable that the observed tendencies were caused by the substitution of Mn^{4+} cations with both Ni^{2+} and Fe^{2+}. Moreover, hardly any difference between the FTIR spectra recorded for spinels prepared using different synthesis methods was observed. For the EDTA-derived samples no band shift was observed for lower concentrations of dopants, whereas for the SSR-derived specimens a band shift was noticeable and more pronounced for higher concentrations. Furthermore, the overall shift is slightly more pronounced for EDTA-derived spinels (max. 13 cm^{-1}) than for SSR-derived ones (max. 10 cm^{-1}). In addition, all bands shifted slightly towards lower wavenumbers for SSR-derived samples, which may originate from lower overall covalency – of all constitutent cations, Mn^{3+} was characterized by the highest N-V parameter and thus the lowest covalency, which suggests slightly higher concentration of these cations after the SSR process. Apart from the ν_1 and ν_2 modes, several additional bands – modes at ca. 695, 455 and 430 cm^{-1} (α-

Mn_2O_3 [64], mostly for SSR), 500 cm^{-1} (MnO_x [65]), as well as 630 and 520 cm^{-1} (CuO [66,67]) – can be observed, which is consistent with the XRD results (Fig. 4). In the case of the MnO_x bands, the much higher sensitivity of FTIR compared to XRD explains why no corresponding peaks are seen in the XRD patterns.

As far as FIR range is concerned, two more regions of absorption can be seen for bands ν_3 and ν_4. The first of these was determined based on the presence of a very broad band in the 325-295 cm^{-1} range. Even though it differs for the EDTA-derived samples of 0.1Ni and 0.3Ni, it is very difficult to provide an informed explanation for this, since the ν_3 mode is dependent on cations from both tetrahedral and octahedral sites [57,58], and numerous bands originating from Mn oxides can be found within this region [64]. Emphasis should therefore be placed on the ν_4 band, which is largely dependent on the mass of tetrahedral cations [57]. In this work, two modes can be seen at ca. 163 and 147 cm^{-1}, which strongly suggest the occurrence of two types of cations at tetrahedral sites – lighter Mn^{2+} cations found at higher wavenumbers and heavier Cu^{+} cations found at lower ones [57,58]. It is worth noting that no shift was observed for either band, which indicates Ni and Fe substitution at octahedral sites only.

3.6. XPS measurements

Fig. 6 shows high-resolution XPS spectra for Cu2p, Mn2p, Ni2p and Fe2p regions. The Cu2p spectra presented a characteristic spin-orbit doublet. This doublet was deconvoluted into two pairs and additional satellite peaks. The positions of peak pairs and presence of characteristic satellite peaks indicate a mix of Cu^{1+} and Cu^{2+} on the surface of the prepared samples [68–70]. It was possible to deconvolute the spectra recorded for Mn2p region into two doublets corresponding to Mn^{3+} and Mn^{4+} valence states [71–73].

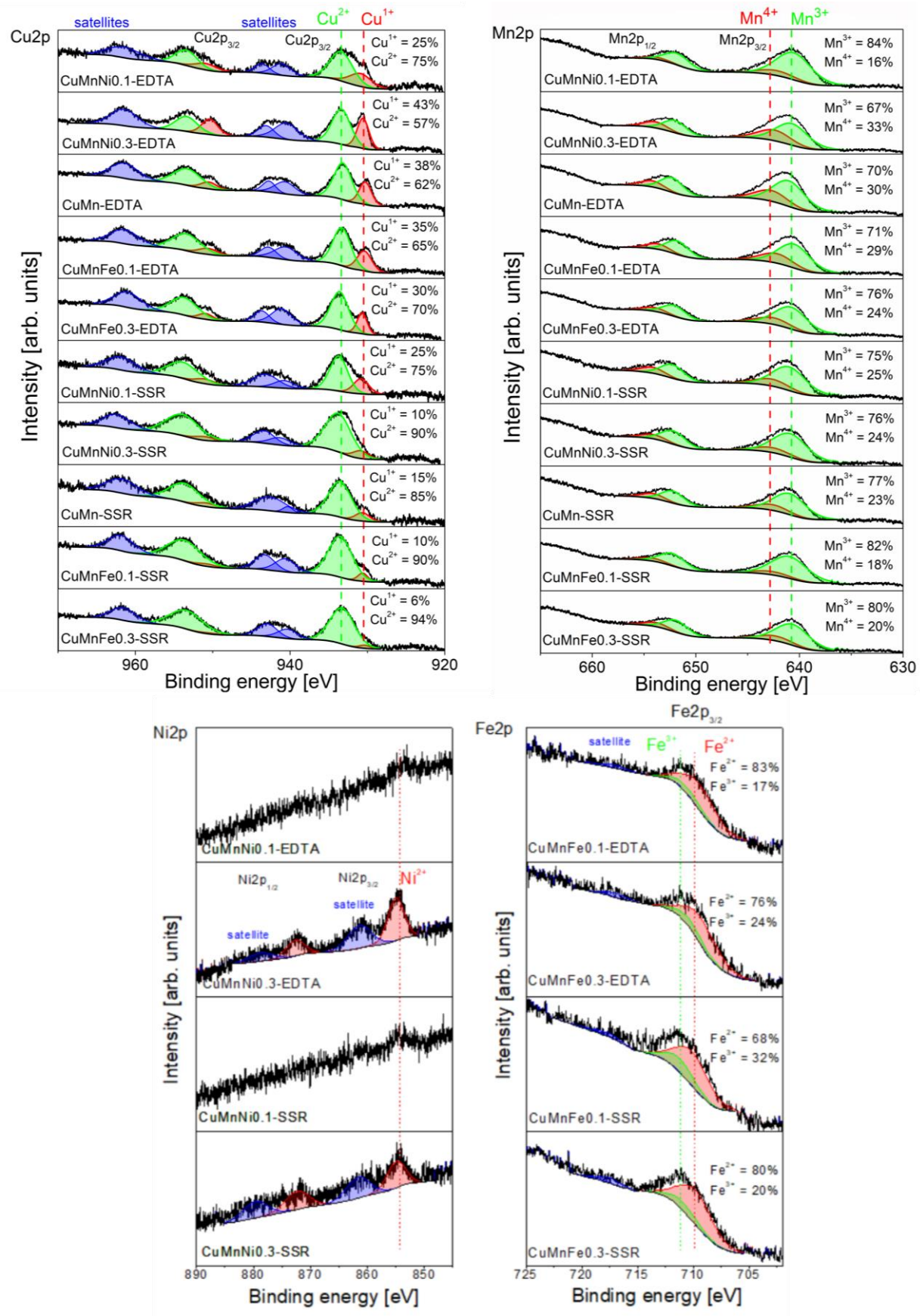

Fig. 6. XPS spectra recorded for Cu2p, Mn2p, Ni2p and Fe2p regions.

The doublet recorded for Ni2p spectra can be attributed to the Ni^{2+} state [74]. The signal was clear for samples with the composition of 0.3Ni, while for samples with the composition of 0.1Ni it was almost imperceptible. The measured spectra for Fe2p were deconvoluted into two peaks corresponding to a mix of Fe^{2+} and Fe^{3+} compounds and a characteristic satellite peak [74]. It should be noted that Fe^{3+} ions were only observed on the oxidized surface of the tested materials. During IR measurements, no Fe^{3+} ions were detected.

Taking into consideration the effect of the applied synthesis method and the introduced dopants on the discussed ions, it can be concluded that they affect the ratios of the Cu^{+}/Cu^{2+} and $Mn^{3+/}Mn^{4+}$ cations. Generally, the EDTA method allows a higher content of Cu^{+} ions to be obtained at the expense of Cu^{2+} ions and a higher content of Mn^{4+} ions at a reduced Mn^{3+} content. Since electrical conduction in spinels occurs mainly via electron hopping between the $Mn^{3+/}Mn^{4+}$ ion pair, increased Mn^{4+} content may translate to higher electrical conductivity. In addition, in Cu-Mn-O spinels, the introduction of copper increases the amount of formed Mn^{4+} ions, simultaneously generating Cu^{+} ions due to charge compensation. It was also observed that the introduction of the Ni^{2+} admixture, especially in larger amounts, usually contributes to an increased concentration of Mn^{4+} ions. On the other hand, for the introduced Fe^{2+} ions, the share of Mn^{4+} was lower compared to the sample without the addition of the admixture (CuMn-EDTA, CuMn-SSR).

3.7. Microstructural characterization of the sinters

Fig. 7 presents the SEM images of the cross-sections of sinters with different compositions and obtained from powders synthesized via the two methods and thermally treated for 2 h in air at 1000°C.

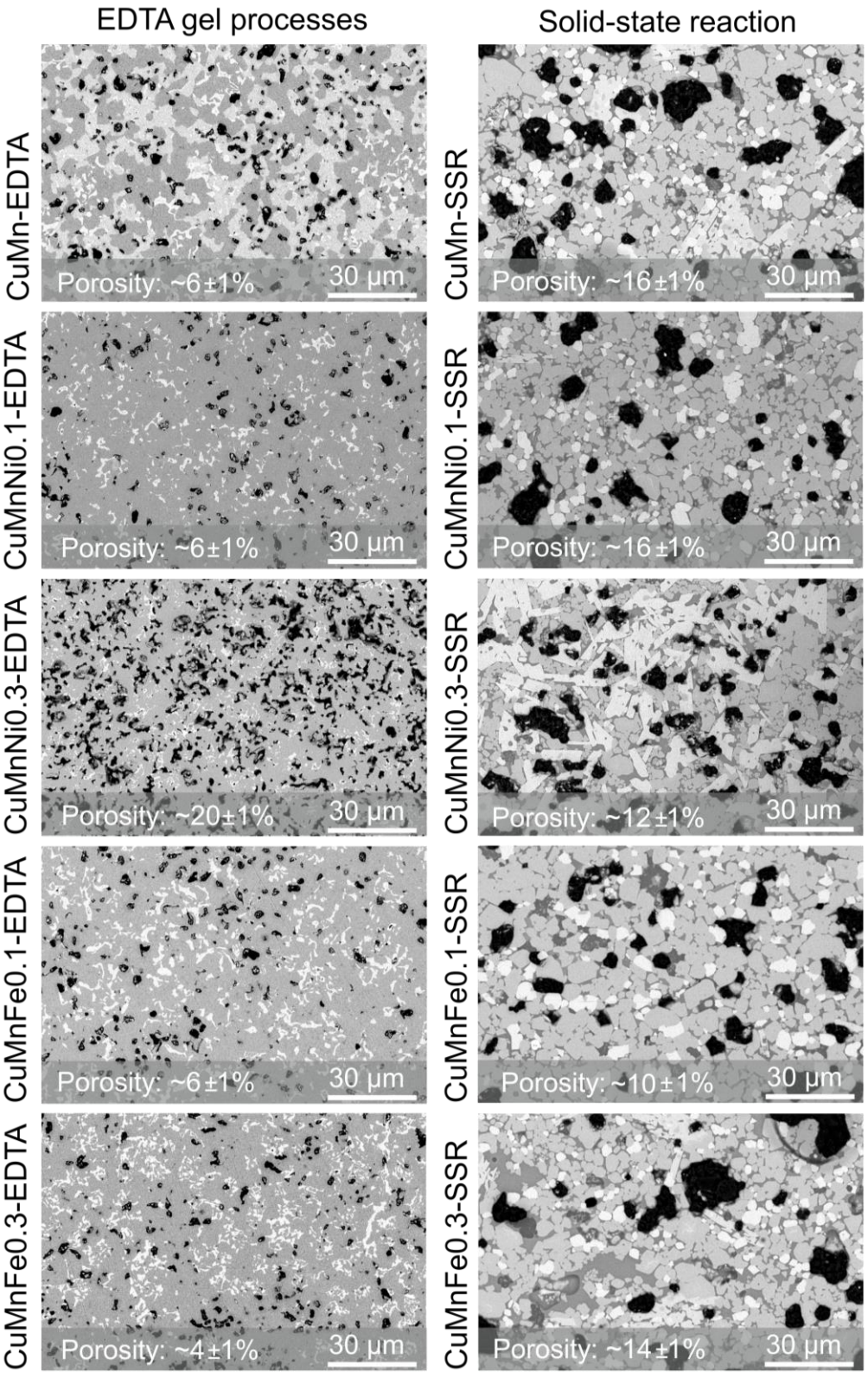

Fig. 7. SEM images of cross-sections of polished sinters prepared from powders obtained via EDTA gel processes or the solid-state reaction method and sintered in air at 1000°C for 2 h.

These images show that the synthesis method significantly affects sinter morphology. The sinters obtained from the powders synthesized via solid-state reaction exhibited a more complex microstructure than those obtained from the powders prepared using EDTA gel processes. First of all, in the case of former the spinel phase matrix was not continuous. Instead, this phase was separated by numerous grain boundaries or inclusions of secondary phases. On the other hand, the EDTA-powder-based sinters exhibited a continuous spinel phase matrix without any visible grain boundaries between the spinel grains.

The only exception was the CuMn-EDTA sample. The results of the EDS chemical analysis carried out for this sample (Fig. 8) revealed the likely presence of two spinel phases. The first one was a phase also found in the other samples, namely the Mn-rich spinel (darker areas in Fig. 8), while the second one was the Cu-rich spinel (brighter areas in Fig. 8).

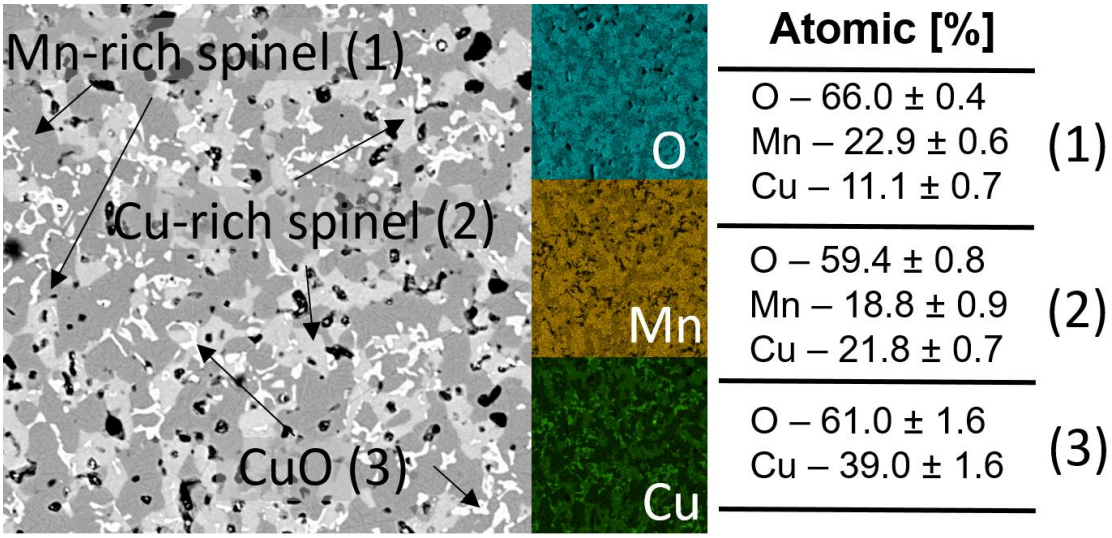

Fig. 8. SEM image of the cross-section of polished CuMn-EDTA sinter and the results of EDS chemical analyses conducted for the indicated areas.

It should be noted that this was observed only for the undoped spinel, which leads to the conclusion that introduction of Ni or Fe dopants can lead to the stabilization of the Mn-rich spinel phase when such processing conditions are applied. Furthermore, the SEM images in Fig. 7 indicate that the CuO that had been detected via XRD had a different distribution

depending on the powder synthesis method. For the solid-state reaction method, the CuO phase formed larger and approximately oval grains dispersed in spinel matrices, while for the EDTA gel processes CuO grains were likewise evenly distributed in spinel matrices, but they are much smaller and had a far less regular shape. Another difference between the sinters is their porosity.

Sinters based on the powders prepared via the solid-state reaction method exhibited higher (~10-16%) porosity in comparison to almost all sinter samples prepared from the powders synthesized via EDTA gel processes (~4-6%). The only exception was the CuMnNi0.3-EDTA sample with a porosity of ~20%, which can be attributed to its poorer sinterability, as indicated by the dilatometric results shown in Fig. 3A. Additionally, the pores in the sinters based on the powders synthesized using the solid-state reaction method were less numerous but much larger than those observed for the sinters based on the powders prepared using EDTA gel processes. These results can be compared with those reported in the available literature.

Ignaczak *et al.* [39] investigated $Mn_{1.7}Cu_{1.3-x}Fe_xO_4$ with different Fe content; the samples were sintered for 2 h in air at different temperatures, and the determined porosity values were as follows: 900°C – ~40-47%, 1000°C – ~19-30%, and 1100°C – 5-17%. Waluyo *et al.* [33] investigated $Cu_xMn_{3-x}O_4$ (x=1-1.5) sintered for 5 h in air at 1000°C, and observed a porosity of ~5-7%. Bobruk *et al.* [47] studied $Cu_{1.3}Mn_{1.7}O_4$ sintered for 2 h in the air at 1120°C and applied different powder calcination conditions; they reported a porosity of ~11-12%. Hosseini *et al.* [13] determined a porosity of ~6-8% for $Cu_xMn_{3-x}O_4$ spinels (where $0.9 \leq x \leq 1.3$) sintered for 2 h in air at 1250°C.

As mentioned when discussing the conducted XRD studies, phase composition also differed depending on the synthesis method. However, even though the spinel and CuO phases could clearly be identified in the presented SEM images, it was impossible to locate

the Mn_2O_3 phase in the sinters based on powders prepared using the solid-state reaction method. One of the possible explanations is that Mn_2O_3 was mixed with the spinel phase, making it impossible to optically distinguish between the two phases. Another feature unique to this group of sinters was the presence of elongated, nearly rectangular grains that were not evenly distributed across the entire sample. Their placement differed depending on the dopant type and content.

Fig. 9 presents a large-scale SEM image of a region in the CuMnFe0.1-SSR sinter, located on the border of areas with and without such grains, and for comparison an image of the CuMnFe0.1-EDTA sinter, using the same scale. Additional magnification was applied in order to conduct EDS chemical analyses of the regions considered most noteworthy.

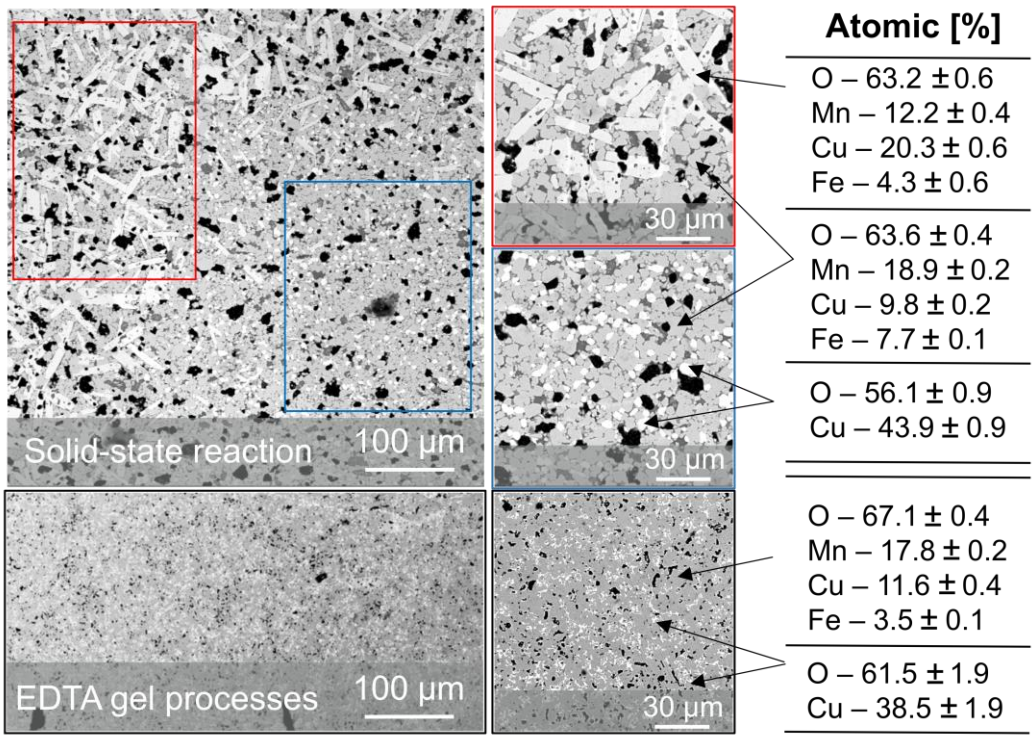

Fig. 9. SEM images of cross-sections of polished CuMnFe0.1-SSR and CuMnFe0.1-EDTA sinters and the results of EDS chemical analyses conducted for the indicated areas.

The chemical composition of these elongated grains was found to be similar to those of the Cu-rich spinel phase found in the CuMn-EDTA sinter shown in Fig. 8. As mentioned, the

distribution of these grains was uneven. For the undoped sample and for both samples doped with Ni, these elongated grains were less numerous and could be found predominantly near the edge of the sinters, whereas for the Fe-doped sinters they could be found across the entire body of each sample.

In conclusion, microstructure was found to have significant influence on those properties of the investigated materials that are relevant to their potential application. In this respect, the EDTA gel processes method seems to be more appropriate for the following reasons: i) it yielded a more homogeneous microstructure and allowed the formation of continuous spinel matrices, which should provide high electrical conductivity, ii) with the exception of CuMnNi0.3-EDTA, the obtained material had fewer pores and these pores were smaller, which should ensure that the deposited coating is dense and can effectively inhibit the formation of volatile Cr compounds, iii) the dopants in the corresponding samples had a more even distribution, which should effectively stabilize the cubic spinel phase in the target temperature ranges.

3.8. Electrical conductivity of the sinters

When discussing DC electrical conductivity in spinel materials, it should be noted that this property is related to the presence of transition metal cations at different valence states in octahedral sites. Therefore, the mechanism of electrical conduction can be represented mainly by the hopping of electrons between nearest cations [75]. It is a well-known fact that manganite-based spinels contain a certain amount of Mn^{4+} ions [23]. In these spinels, electron hopping occurs between Mn^{3+} and Mn^{4+} ions due to their strong tendency to occupy octahedral sites [76]. $Cu_xMn_{3-x}O_4$ spinels ($0.9 \leq x \leq 1.3$) also exhibit conduction based on an electron hopping mechanism. However, in the presence of copper ions, this mechanism may be expressed using the following equation [13]:

$$Cu^{2+} + Mn^{3+} \rightarrow Cu^{+} + Mn^{4+} \quad (4)$$

This explains the significant increase in the electrical conductivity of $Cu_xMn_{3-x}O_4$, observed when copper content in the range of $0.9 \leq x \leq 1.3$ increases [13]. With higher copper content, the number of Mn^{3+}/Mn^{4+} pairs increases. At the same time, the average distance between available hopping sites is reduced, facilitating the transfer of electrons and thereby increasing conductivity [13,77].

To evaluate the influence of the synthesis method and the applied Fe and Ni dopants on the electrical conductivity of the $Cu_{1.3}Mn_{1.7}O_4$ spinel, measurements were carried out in the temperature range of 850-300°C. The results are presented in Figs 10A and 10B. To reduce the effect of pores, conductivity was corrected for porosity using the Brueggemann model [53] expressed by Eq. 2. In addition, Figs 10C and 10D shows the values of the Seebeck coefficient for all tested materials.

The presented plots show that the CuMn-EDTA, CuMnNi0.1-EDTA, CuMnNi0.3-EDTA and CuMnFe0.1-EDTA spinels (Fig. 10A) exhibit their maximum electrical conductivity at temperatures in the range of about 706-750°C. The CuMn-EDTA sample reached its highest electrical conductivity of 142 S/cm at ~750°C, while the corresponding values for the CuMnNi0.1-EDTA, and CuMnNi0.3-EDTA were 136 and 163 S/cm at ~730 and ~706°C, respectively. For the sinter with the lower Fe content (CuMnFe0.1-EDTA), the maximum measured electrical conductivity was equal to 150 S/cm at ~730°C. Below the maximum, conduction was thermally activated, whereas above the maximum, conductivity decreased with increasing temperature. The sample with the higher iron content – CuMnFe0.3-EDTA (Fig. 10A) – and all samples based on powders obtained via the solid-state reaction – CuMn-SSR, CuMnNi0.1-SSR, CuMnNi0.3-SSR, CuMnFe0.1-SSR, and CuMnFe0.3-SSR (Fig. 10B) – exhibited regular thermally activated behavior across the full range of measurement temperature.

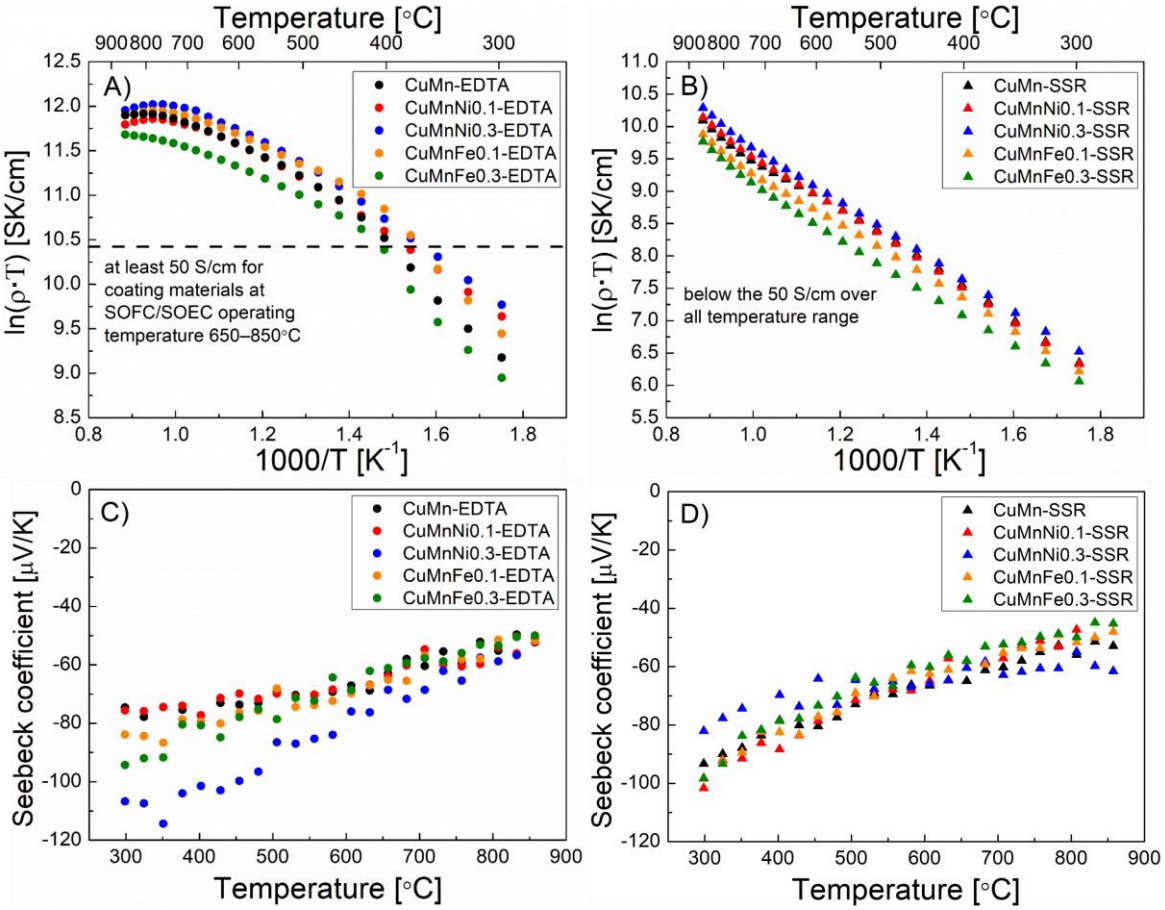

Fig. 10. Electrical conductivity of spinels based on powders prepared using A) EDTA gel processes or B) solid-state reaction and the corresponding Seebeck coefficients: C) and D).

As far as the influence of the powder synthesis method on the electrical conductivity of Cu-Mn-O spinels, it can be concluded that the application of EDTA gel processes yields sinters with significantly higher conductivity. Table 5 lists the conductivity values measured for the discussed sinters at 800°C – a temperature that reflects the anticipated operating conditions of a SOEC/SOFC interconnect. Depending on the dopant type and content, the included values are 7-10 times higher in the case of spinels based on powders synthesized via EDTA gel processes than the sinters obtained from powders prepared using solid-state reactions. Electrical conductivity in spinel materials is a complex phenomenon and can be influenced by many factors. In the present study the fact that the differences in the spinels'

conductivity were so high can be explained mainly by the differences in sample microstructure. However, the different ratios of cations in the obtained materials – as indicated by the conducted XPS investigations – may also affect the observed conductivity values to a certain degree. As already shown in Fig. 7, applying two different synthesis methods is associated with significant differences in the sinter microstructure.

Table 5. Electrical conductivity (σ) and activation energy of electrical conductivity (E_a), as determined for the studied spinels at 800°C.

Sample type	σ at 800°C [S/cm]	E_a [eV]	
		300-420°C	450-730°C
CuMn-EDTA	137	0.41	0.20
CuMnNi0.1-EDTA	128	0.29	0.19
CuMnNi0.3-EDTA	150	0.29	0.20
CuMnFe0.1-EDTA	140	0.41	0.17
CuMnFe0.3-EDTA	106	0.44	0.17
Sample type	σ at 800°C [S/cm]	E_a [eV]	
		300-680°C	700-850°C
CuMn-SSR	17	0.34	0.43
CuMnNi0.1-SSR	18	0.35	0.43
CuMnNi0.3-SSR	21	0.33	0.43
CuMnFe0.1-SSR	14	0.33	0.42
CuMnFe0.3-SSR	12	0.33	0.45

The EDTA gel processes method yields sinters with a spinel phase that forms continuous, highly conducting matrices in which less conductive CuO inclusions can be found. This is not true when the solid-state reaction is applied for powder synthesis. In this case the microstructure of the obtained sinters is characterized by numerous grain boundaries, mostly between different phases. The scattering of electrons at these grain boundaries hinders their transport, leading to a significant decrease in electrical conductivity [78]. Moreover, the presence of poorly conducting secondary phases and microstructural defects such as pores or cracks can further reduce electrical conductivity [79]. However, in this case there are at least

two reasons why these particular microstructural features are unlikely to be the cause of the observed differences. The secondary phases form rather isolated inclusions (mainly CuO) scattered in the spinel matrices – continuous for EDTA gel processes and non-continuous for solid-state reactions. Moreover, the differences in the secondary phase content determined for nearly all sinters regardless of the powder synthesis methods are by no means dramatic (Tables 3 and 4). As mentioned earlier, some differences in pore size, shape and distribution can be noticed when comparing spinels based on powders obtained using the two methods. However, although these differences certainly contribute to the differences in electrical conductivity to some degree, they are again not the main reason. This is especially evident for sample CuMnFe0.3-EDTA, which has the highest porosity, but also the highest conductivity.

With regard to the influence of the dopant on electrical conductivity (Table 5), it can be observed that the highest and the lowest values were obtained for the spinels with 0.3 of Ni and Fe, respectively, regardless of the synthesis methods. The addition of 0.3Ni improved electrical conductivity by ~9.5% for the samples based on EDTA gel processes and ~23.5% for those based on solid-state reactions, whereas the introduction of 0.3Fe decreased conductivity by ~22.5% and ~29.5%, respectively. The lowest conductivity of the CuMnFe0.3-EDTA spinel can be attributed to the partial transformation of the highly conducting cubic spinel structure into a poorly conducting tetragonal one, observed for the higher Fe content [39]. On the other hand, the lower amount of each dopant did not affect the electrical conductivity of doped spinels in a very pronounced way (with exception of CuMnFe0.1-SSR), increasing or decreasing it only slightly. For EDTA gel processes, the introduction of 0.1Ni decreased electrical conductivity by ~7% and adding 0.1Fe increased it by ~2%; in the case of the samples for which the preparation involved solid-state reactions, the opposite effect was observed (0.1Ni) increases conductivity by ~6% and 0.1Fe decreases

it by ~17,7%). It should be noted that for some doped spinels, this change in electrical conductivity was within the error margin (± 5%).

The obtained results are in good agreement with literature data. For example, Hosseini *et al.* [13] obtained a $Cu_{1.3}Mn_{1.7}O_4$ spinel with an electrical conductivity of ~140 S/cm at 750°C after 2 h of sintering in air at 1250°C. Bobruk *et al.* [47] reported a conductivity of ~90-105 S/cm for $Cu_{1.3}Mn_{1.7}O_4$, depending on the powder calcination temperature. Ignaczak *et al.* [39] showed that increasing the iron content generally leads to a decrease in the electrical conductivity of a Cu-Mn-O spinel sintered for 2 h in air at 900°C across the temperature range in which maximum conductivity was observed (600-750°C). The only exception was addition of 0.1Fe, which slightly improved conductivity; however, according to the authors the observed improvement was within the error margin. The situation changed at 800°C, at which the conductivity of the $CuMn_{1.7}Fe_{0.3}O_4$ spinel was higher (~140 S/cm) than that of $Cu_{1.3}Mn_{1.7}O_4$ and $Cu_{1.2}Mn_{1.7}Fe_{0.1}O_4$ (~130 S/cm and ~134 S/cm, respectively). It should be noted that the cited results were obtained after correcting for porosity. In the same study, the authors evaluated the electrical conductivity of the following samples: $Cu_{1.3}Mn_{1.7}O_4$, $Cu_{1.2}Mn_{1.7}Fe_{0.1}O_4$ and $CuMn_{1.7}Fe_{0.3}O_4$. When sintered at 1000°C, these samples exhibited electrical conductivity values of ~48 S/cm, ~75 S/cm, and ~95 S/cm, respectively. The corresponding values after sintering these spinels at 1100°C were ~96 S/cm, ~93 S/cm, and ~65 S/cm. In this case, no correction for porosity was made. It was also indicated in this study that high Fe content ($Cu_{0.8}Mn_{1.7}Fe_{0.5}O_4$) leads to a significant reduction in electrical conductivity at all sintering temperatures, mainly due to the transformation into a poorly conducting tetragonal phase. With regard to Ni as a dopant, Joshi and Petric [50] reported improved conductivity when Cu was substituted with Ni, forming $Cu_{0.77}Ni_{0.45}Mn_{1.78}O_4$ (~116 S/cm), in comparison to the initial $Cu_{1.18}Mn_{1.82}O_4$ (~60 S/cm). The authors postulated that Ni

can significantly contribute to the electrical conductivity of the $Cu_xNi_{1-x}Mn_2O_4$ system when $0.8 \geq x \geq 0.6$.

The determined values of the Seebeck coefficient for all tested sinters in the entire measurement temperature range (Figs. 8C and 8D) varied between -40 and -120 μV/K for both synthesis methods, with no significant differences between them.

The negative values of the Seebeck coefficient show that the studied materials exhibit an n-type conductivity. Assuming a negligible contribution of both ionic and electron-hole conductivity components, the estimated concentrations of electrons, n, were determined based on the following relationship:

$$\alpha = -\frac{k}{e}\left[\ln\left(\frac{N}{n}\right) + A\right] \tag{5}$$

where k – Boltzmann constant [J/K], N – density of states for electrons [1/cm^3], A – kinetic parameter related to electrons [-], e – elementary charge [C] and n – concentration of electrons [1/cm^3]. Assuming that parameter A is equal to zero – as proposed in [80] – the concentration of charge carriers expressed as an atomic percent, Eq. 6 takes the form of the equation below:

$$n[at\%] = 100 \cdot \exp\left[\frac{\alpha \cdot e}{k}\right] \tag{6}$$

Calculation show that n changes from ca. 30 at.% at 300°C to 56 at.% at 800°C (Table 6).

At this research stage, it can be concluded that electrical conduction in the investigated sinters is predominantly determined by electron carriers. Moreover, taking into consideration the different valency of ionic components of the material (Cu^+/Cu^{2+}; Mn^{3+}/Mn^{4+}), the above-postulated (Eq.4) hopping mechanism of charge transport is likely.

Table 6. Concentrations of quasi-free electrons for selected samples, estimated from Seebeck coefficients.

T [°C]	Atomic percent [%]					
	CuMn-EDTA	CuMnNi0.3-EDTA	CuMnFe0.3-EDTA	CuMn-SSR	CuMnNi0.3-SSR	CuMnFe0.3-SSR
800	52.73	50.55	53.82	52.22	52.87	56.08
725	52.56	48.65	50.52	51.02	48.83	54.89
575	44.75	37.73	47.39	46.35	45.95	50.13
300	42.09	28.98	33.50	33.88	38.60	31.94

The $\ln(\sigma T) = f(1/T)$ dependence of electrical conductivity presented in Figs 10A and 10B suggests that this process is thermally activated. Consequently, the activation energies of electrical conductivity for the samples were calculated by applying the Nernst-Einstein dependence [39]:

$$\ln(\sigma \cdot T) = \ln \sigma_o - \frac{E_a}{k \cdot T} \tag{7}$$

where: σ – electrical conductivity [1/(Ω·cm)], σ_o – pre-exponential factor [1(Ω·cm·K)], E_a – activation energy of electrical conductivity [eV], k – Boltzmann constant [eV/K] and T – absolute temperature [K].

The results are listed in Table 5. The spinels prepared from both the powders synthesized using the EDTA gel processes and those obtained via the solid-state reaction method exhibited a visible change in slope; however, in the case of the former, this change was more evident, while for the latter it was more subtle. Consequently, activation energies were calculated for two temperature ranges: 300-420°C and 450-730°C for EDTA gel processes and 300-680°C and 700-850°C for solid-state reactions. For the EDTA-powder-based spinels a transition point at which electrical conductivity level step-changed could clearly be distinguished. This transition was observed at a temperature of around 400°C and

was the result of the transformation of the tetragonal phase to cubic spinel (Fig. 10A). This effect was not pronounced in the case of the other group of spinels (Fig. 10B).

In general, EDTA-powder-based spinels exhibited higher activation energies across ranges of lower temperatures. In this temperature range, Ni-doped spinels had lower activation energies than undoped and Fe-doped spinels. In the ranges of higher temperatures, activation energies decreased, and were at a similar level for all spinel materials. For the solid-state reaction spinels, the change in the slope occurred at higher temperatures and was more subtle. In terms of the activation energy of these spinels, the observed tendencies were the opposite of those described for the EDTA-powder-based spinels. In this case, lower-temperature regions were associated with lower activation energies, whereas at higher temperatures, higher activation energy values were observed. It should be noted that the determined activation energies were consistent with the typically reported values [13,39,47,81]. The differences between activation energy values for low- and high-temperature ranges may be attributed to the concentration of charge carriers and the microstructure (grain size and distribution, presence or absence of grain boundaries) of the studied spinels [47,82].

Given that a coating material for SOFC/SOEC applications should exhibit an electrical conductivity of above 50 S/cm at the target operating temperature range (650-850°C) [13], it can be noted that all studied EDTA-powder-based spinel materials are suitable for this purpose. Furthermore, these materials exhibit high conductivity at temperatures as low as 600°C, which it is worth emphasizing in light of the recent strong tendency to reduce the SOFC/SOEC operating temperature to this level [5]. On the other hand, the conductivity of the spinels prepared using powders synthesized via the solid-state reaction precludes their application at either operating temperature.

4. Potential application as a protective coating on SOFC/SOEC interconnects

Due to its properties, the Cu-Mn-O spinel is considered for many applications, including as a material for protective-conducting coatings on metallic interconnects for SOFCs/SOECs. In fact, spinels – especially $(Mn,Co)_3O_4$ ones – are already considered some of the best materials for this purpose. Despite the favourable properties of such coatings, their use is severely limited due to the presence of cobalt, which has been classified as a carcinogenic element. Consequently, there is a clear tendency to replace Co with Cu not just in protective coatings for metallic interconnects but also in next-generation electrodes dedicated for SOFCs/SOECs [83]. Few studies on manganese-copper protective coatings have been conducted thus far [33,40,51,84–86], and the evaluated oxidation times were relatively short in most of them.

To optimize the application of Cu-Mn-O based spinels as coating materials for SOFC/SOEC interconnects, it is necessary to stage long-term oxidation studies. The results that have been presented in this work can be considered a starting point for the development of spinel coatings with the desired physicochemical characteristics for long-term oxidation studies of steel/coating systems.

Fig. 11 presents mass gain as a function of oxidation time for the unmodified Nirosta 4016/1.4016 ferritic steel and the steel sample modified with a $Cu_{1.25}Mn_{1.65}Ni_{0.1}O_4$ spinel coating. Both samples had been oxidized for 2000 h in air at 800˚C.

As can be seen, significant mass gain is observed for the unmodified steel up to about 600 h, after which its mass decreases due to scale spallation after the thermal treatment (inset in Fig. 11). In contrast, steel modified with the spinel coating maintains its protective properties throughout the entire corrosion process.

Fig. 12 presents a SEM micrograph as well as EDS element distribution maps for a $Cu_{1.25}Mn_{1.65}Ni_{0.1}O_4$ ceramic coating deposited on the Nirosta 4016/1.4016 ferritic stainless

steel via electrophoresis. This coating/steel layered system had undergone 2000 h of high-temperature oxidation in air at 800°C.

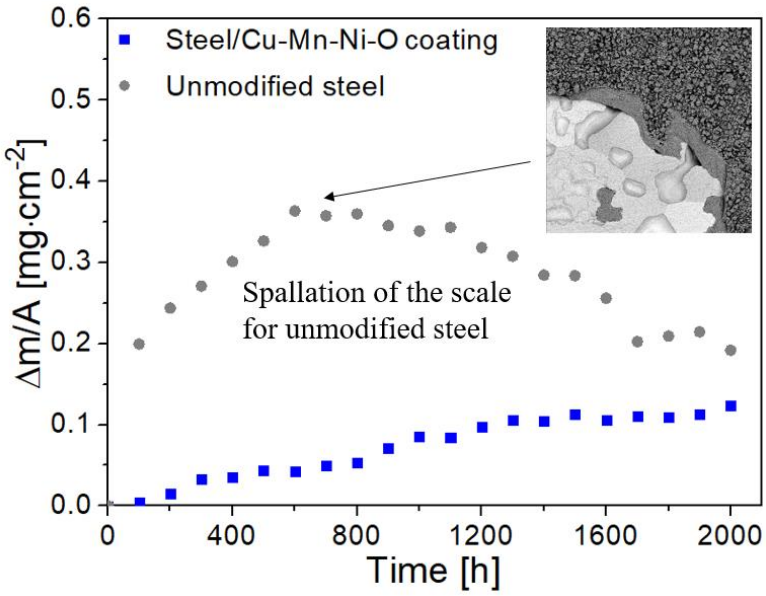

Fig. 11. Oxidation kinetics of the unmodified steel and steel modified with a Cu-Mn-Ni-O spinel coating after 2000 h in air at 800˚C.

Inset: morphology of the oxidized unmodified steel, illustrating the spallation process.

As a result of the conducted long-term oxidation test, a reaction layer composed predominantly of Cr_2O_3 had formed between the substrate and the ceramic coating. This layer had an average thickness of ~1.7 μm. The coated steel exhibited an ASR of ~0.023 Ω·cm^2 at 800°C, which is less than half of the ASR of unmodified steel (~0.049 Ω·cm^2). Additionally, the low porosity of the coating allowed Cr-diffusion to be significantly reduced via the formation of an effective layer protecting the chromium-sensitive elements of SOFC/SOEC devices (electrodes) against the formation of volatile chromium compounds. Last but not least, the presented coating was characterized by good adhesion to the ferritic steel, with no cracks and spallation observed across the tested sample.

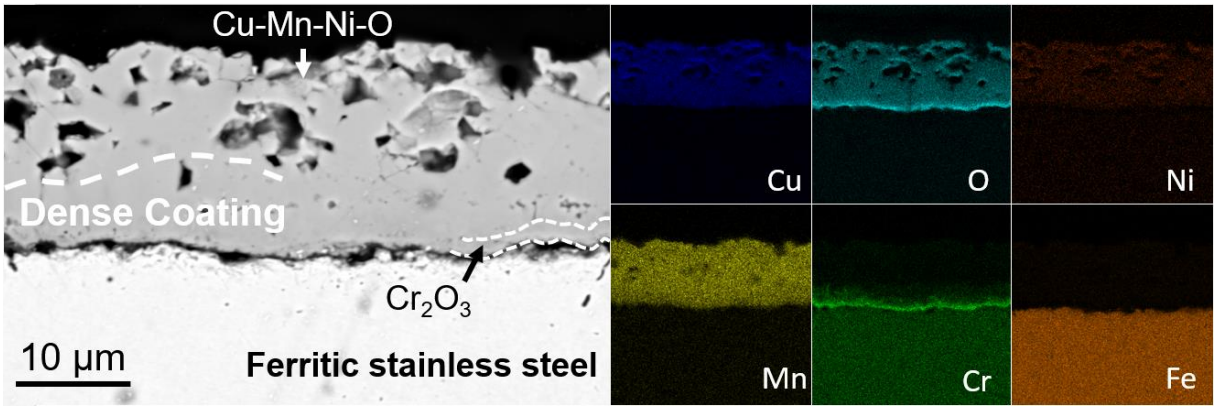

Fig. 12. SEM micrograph of a polished cross-section of a Cu-Mn-Ni-O spinel coating electrophoretically deposited on ferritic stainless steel after 2000 h of oxidation in air at 800°C and the EDS element distribution map for this layered system.

The above-described physicochemical properties of the coating/steel layer system can be of fundamental importance for the durability of an intermediate-temperature SOEC/SOFC, which has an expected operating time of 40000 h.

5. Conclusions

Spinel powders with the composition of $Cu_{1.3-0.5x}Mn_{1.7-0.5x}M_xO_4$ (where M=Ni, Fe; x=0, 0.1, 0.3) were synthesized using EDTA gel processes and solid-state reaction methods. Of the two tested methods, EDTA gel processes proved to be much more effective at obtaining spinel with desirable properties. The most important parameter, namely electrical conductivity at 800°C, was 7-10 times greater for EDTA-powder-based sinters compared with the corresponding sinters based on powders obtained via the solid-state reaction. This can mostly be attributed to the differences in microstructure.

The addition of Ni and Fe affects the properties of the $Cu_{1.3}Mn_{1.7}O_4$ spinel in different ways. In general, a low amount of these dopants, i.e. 0.1 Ni or Fe, does not have considerable influence on the spinels' properties. On the other hand, a higher amount of nickel (0.3Ni)

improves the electrical conductivity of $Cu_{1.3}Mn_{1.7}O_4$, whereas a higher amount of iron (0.3Fe) reduces it. Moreover, when added in this amount, iron can cause the transformation of the cubic spinel phase into the tetragonal one.

To conclude, all spinels obtained from powders synthesized using EDTA gel processes exhibit an electrical conductivity of over 50 S/cm at the current SOFC/SOEC operating temperature range of 650-850°C. Based on the obtained data, electrical conduction in the investigated sinters can be concluded to be determined predominantly by electron carriers. This conductivity value is the threshold for potential coating materials on metallic interconnects. These spinel materials are also suitable for operation at even lower temperatures (~600°C), as per the current trends in SOFC/SOEC devices. On the other hand, spinels based on powder obtained via solid-state reactions were characterized by electrical conductivity that was below this threshold across the entire operating temperature range. The high electrical conductivity of the spinels prepared from powders synthesized using EDTA gel processes and their low porosity makes them very good coating materials for the surface modification of SOFC/SOEC metallic interconnects, which was validated by performing long-term oxidation tests of a layered system in which this spinel was deposited electrophoretically on a ferritic stainless steel substrate.

Acknowledgements

Research project supported by program "Excellence initiative – research university" for the University of Science and Technology (ŁM). Funding of National Science Centre (NCN) project No. 2021/41/B/ST8/02187 is also gratefully acknowledged (TB).

Highlights:

Cu-Mn-O spinel microstructure can be engineered via appropriate powder synthesis.

EDTA-powder-based spinels exhibit electrical conductivity >50 S/cm above 400°C.

Solid-state-reaction-based spinels have low electrical conductivity over 300-850°C.

Higher Ni content improves the conductivity of spinels, whereas Fe decreases it.

Cu-Mn-O spinels are suitable coating materials for SOEC/SOFCs metallic interconnects.

References

[1] M. Ni, M.K.H. Leung, D.Y.C. Leung, Technological development of hydrogen production by solid oxide electrolyzer cell (SOEC), Int. J. Hydrogen Energy. 33 (2008) 2337–2354. https://doi.org/10.1016/j.ijhydene.2008.02.048.

[2] M.A. Laguna-Bercero, Recent advances in high temperature electrolysis using solid oxide fuel cells: A review, J. Power Sources. 203 (2012) 4–16. https://doi.org/10.1016/j.jpowsour.2011.12.019.

[3] W.J. Quadakkers, J. Piron-Abellan, V. Shemet, L. Singheiser, Metallic interconnectors for solid oxide fuel cells- A review, Mater. High Temp. 20 (2003) 115–127. https://doi.org/10.3184/096034003782749071.

[4] W.Z. Zhu, S.C. Deevi, Development of interconnect materials for solid oxide fuel cells, Mater. Sci. Eng. A. 348 (2003) 227–243. https://doi.org/10.1016/S0921-5093(02)00736-0.

[5] J.C.W. Mah, A. Muchtar, M.R. Somalu, M.J. Ghazali, Metallic interconnects for solid oxide fuel cell: A review on protective coating and deposition techniques, Int. J. Hydrogen Energy. 42 (2017) 9219–9229. https://doi.org/10.1016/j.ijhydene.2016.03.195.

[6] M.A. Hassan, O. Bin Mamat, M. Mehdi, Review: Influence of alloy addition and spinel coatings on Cr-based metallic interconnects of solid oxide fuel cells, Int. J. Hydrogen Energy. 45 (2020) 25191–25209. https://doi.org/10.1016/j.ijhydene.2020.06.234.

[7] K. Hilpert, D. Das, M. Miller, D.H. Peck, R. Weiß, Chromium Vapor Species over Solid Oxide Fuel Cell Interconnect Materials and Their Potential for Degradation Processes, J. Electrochem. Soc. 143 (1996) 3642–3647. https://doi.org/10.1149/1.1837264.

[8] Y. Matsuzaki, I. Yasuda, Dependence of SOFC Cathode Degradation by Chromium-Containing Alloy on Compositions of Electrodes and Electrolytes, J. Electrochem. Soc. 148 (2001) A126. https://doi.org/10.1149/1.1339869.

[9] Ł. Mazur, J. Ignaczak, M. Bik, S. Molin, M. Sitarz, Aleksander Gil, T. Brylewski, Effectiveness of a dual surface modification of metallic interconnects for application in energy conversion devices, Int. J. Hydrogen Energy. 47 (2022) 6295–6311. https://doi.org/10.1016/j.ijhydene.2021.11.256.

[10] T. Brylewski, S. Molin, M. Marczyński, Mazur, K. Domaradzki, O. Kryshtal, A. Gil, Influence of Gd deposition on the oxidation behavior and electrical properties of a layered system consisting of Crofer 22 APU and MnCo2O4 spinel, Int. J. Hydrogen Energy. 46 (2021) 6775–6791. https://doi.org/10.1016/j.ijhydene.2020.11.169.

[11] F. Cheng, J. Sun, Fabrication of a double-layered Co-Mn-O spinel coating on stainless steel via the double glow plasma alloying process and preoxidation treatment as SOFC interconnect, Int. J. Hydrogen Energy. 44 (2019) 18415–18424. https://doi.org/10.1016/j.ijhydene.2019.05.060.
[12] A. Petric, H. Ling, Electrical conductivity and thermal expansion of spinels at elevated temperatures, J. Am. Ceram. Soc. 90 (2007) 1515–1520. https://doi.org/10.1111/j.1551-2916.2007.01522.x.
[13] N. Hosseini, F. Karimzadeh, M.H. Abbasi, G.M. Choi, Microstructural characterization and electrical conductivity of Cu xMn3-xO4 (0.9≤x≤1.3) spinels produced by optimized glycine-nitrate combustion and mechanical milling processes, Ceram. Int. 40 (2014) 12219–12226. https://doi.org/10.1016/j.ceramint.2014.04.065.
[14] G. J.B., Magnetism and Chemical Bond, Interscience Publishers Inc. and John-Wiley Inc., New York, 1963.
[15] M.M.S. Sanad, H.A. Abdellatif, E.M. Elnaggar, G.M. El-Kady, M.M. Rashad, Understanding structural, optical, magnetic and electrical performances of Fe- or Co-substituted spinel LiMn 1.5 Ni 0.5 O 4 cathode materials, Appl. Phys. A Mater. Sci. Process. 125 (2019) 1–10. https://doi.org/10.1007/s00339-019-2445-8.
[16] Y. Zhou, S. Sun, J. Song, S. Xi, B. Chen, Y. Du, A.C. Fisher, F. Cheng, X. Wang, H. Zhang, Z.J. Xu, Enlarged Co□O Covalency in Octahedral Sites Leading to Highly Efficient Spinel Oxides for Oxygen Evolution Reaction, Adv. Mater. 30 (2018). https://doi.org/10.1002/adma.201802912.
[17] Y. Liu, J.W. Fergus, K. Wang, C. Dela Cruz, Crystal Structure, Chemical Stabilities and Electrical Conductivity of Fe-Doped Manganese Cobalt Spinel Oxides for SOFC Interconnect Coatings, J. Electrochem. Soc. 160 (2013) F1316–F1321. https://doi.org/10.1149/2.114311jes.
[18] T. Brylewski, W. Kucza, A. Adamczyk, A. Kruk, M. Stygar, M. Bobruk, J. Dąbrowa, Microstructure and electrical properties of Mn1+xCo 2-xO4 (0 ≤ x ≤ 1.5) spinels synthesized using EDTA-gel processes, Ceram. Int. 40 (2014) 13873–13882. https://doi.org/10.1016/j.ceramint.2014.05.106.
[19] M. Bednarz, S. Molin, M. Bobruk, M. Stygar, E. Długoń, M. Sitarz, T. Brylewski, High-temperature oxidation of the Crofer 22 H ferritic steel with Mn1.45Co1.45Fe0.1O4 and Mn1.5Co1.5O4 spinel coatings under thermal cycling conditions and its properties, Mater. Chem. Phys. 225 (2019) 227–238. https://doi.org/10.1016/j.matchemphys.2018.12.090.
[20] Ł. Mazur, S. Molin, J. Dąbek, K. Durczak, M. Pyzalski, T. Brylewski, Physicochemical properties of Mn1.45Co1.45Cu0.1O4 spinel coating deposited on the Crofer 22 H ferritic steel and exposed to high-temperature oxidation under thermal cycling conditions, J. Therm. Anal. Calorim. 147 (2021) 5649–5666. https://doi.org/10.1007/s10973-021-10884-2.
[21] B.K. Park, J.W. Lee, S.B. Lee, T.H. Lim, S.J. Park, C.O. Park, R.H. Song, Cu- and Ni-doped Mn1.5Co1.5O4 spinel coatings on metallic interconnects for solid oxide fuel cells, Int. J. Hydrogen Energy. 38 (2013) 12043–12050. https://doi.org/10.1016/j.ijhydene.2013.07.025.
[22] B. Talic, S. Molin, K. Wiik, P.V. Hendriksen, H.L. Lein, Comparison of iron and copper doped manganese cobalt spinel oxides as protective coatings for solid oxide fuel cell interconnects, J. Power Sources. 372 (2017) 145–156. https://doi.org/10.1016/j.jpowsour.2017.10.060.
[23] I. Thaheem, D.W. Joh, T. Noh, K.T. Lee, Highly conductive and stable Mn 1.35 Co 1.35 Cu 0.2 Y 0.1 O 4 spinel protective coating on commercial ferritic stainless steels for intermediate-temperature solid oxide fuel cell interconnect applications, Int. J.

Hydrogen Energy. 44 (2019) 4293–4303. https://doi.org/10.1016/j.ijhydene.2018.12.173.
[24] H.P. Tseng, T.Y. Yung, C.K. Liu, Y.N. Cheng, R.Y. Lee, Oxidation characteristics and electrical properties of La- or Ce-doped MnCo2O4 as protective layer on SUS441 for metallic interconnects in solid oxide fuel cells, Int. J. Hydrogen Energy. 45 (2020) 12555–12564. https://doi.org/10.1016/j.ijhydene.2020.02.178.
[25] B. Talic, H. Falk-Windisch, V. Venkatachalam, P.V. Hendriksen, K. Wiik, H.L. Lein, Effect of coating density on oxidation resistance and Cr vaporization from solid oxide fuel cell interconnects, J. Power Sources. 354 (2017) 57–67. https://doi.org/10.1016/j.jpowsour.2017.04.023.
[26] S. Molin, P. Jasinski, L. Mikkelsen, W. Zhang, M. Chen, P. V. Hendriksen, Low temperature processed MnCo2O4 and MnCo1.8Fe0.2O4 as effective protective coatings for solid oxide fuel cell interconnects at 750 °C, J. Power Sources. 336 (2016) 408–418. https://doi.org/10.1016/j.jpowsour.2016.11.011.
[27] J. Froitzheim, S. Canovic, M. Nikumaa, R. Sachitanand, L.G. Johansson, J.E. Svensson, Long term study of Cr evaporation and high temperature corrosion behaviour of Co coated ferritic steel for solid oxide fuel cell interconnects, J. Power Sources. 220 (2012) 217–227. https://doi.org/10.1016/j.jpowsour.2012.06.092.
[28] P. Ma, Q. Geng, X. Gao, T. Zhou, S. Yang, G. Liu, Aqueous solution-derived CuMn2O4 ceramic films for spectrally selective solar absorbers, Ceram. Int. 42 (2016) 19047–19057. https://doi.org/10.1016/j.ceramint.2016.09.062.
[29] R. Bayón, G. San Vicente, C. Maffiotte, Á. Morales, Preparation of selective absorbers based on CuMn spinels by dip-coating method, Renew. Energy. 33 (2008) 348–353. https://doi.org/10.1016/j.renene.2007.05.017.
[30] L. Li, G. Jiang, J. Ma, CuMn2O4/graphene nanosheets as excellent anode for lithium-ion battery, Mater. Res. Bull. 104 (2018) 53–59. https://doi.org/10.1016/j.materresbull.2018.03.051.
[31] T. Fukunaga, N. Ryumon, N. Ichikuni, S. Shimazu, Characterization of CuMn-spinel catalyst for methanol steam reforming, Catal. Commun. 10 (2009) 1800–1803. https://doi.org/10.1016/j.catcom.2009.06.001.
[32] C. Zhang, A. Xie, W. Zhang, J. Chang, C. Liu, L. Gu, X. Duo, F. Pan, S. Luo, CuMn2O4 spinel anchored on graphene nanosheets as a novel electrode material for supercapacitor, J. Energy Storage. 34 (2021) 102181. https://doi.org/10.1016/j.est.2020.102181.
[33] N.S. Waluyo, B.K. Park, S.B. Lee, T.H. Lim, S.J. Park, R.H. Song, J.W. Lee, (Mn,Cu)3O4-based conductive coatings as effective barriers to high-temperature oxidation of metallic interconnects for solid oxide fuel cells, J. Solid State Electrochem. 18 (2014) 445–452. https://doi.org/10.1007/s10008-013-2245-6.
[34] X. Chen, P.Y. Hou, C.P. Jacobson, S.J. Visco, L.C. De Jonghe, Protective coating on stainless steel interconnect for SOFCs: Oxidation kinetics and electrical properties, Solid State Ionics. 176 (2005) 425–433. https://doi.org/10.1016/j.ssi.2004.10.004.
[35] S. Obbade, K. Zaidat, C. Rossignol, L. Dessemond, M. mohamed S. Sanad, T. Mattar, M.F. El-Shahat, S.M. Mohamed, Copper and Nickel Substitution Role on the Structural, Thermal and Electrochemical Properties in Two New Mnfe1-X-Ycuxniycoo4 Spinel Protective Layers in Stacked Solid Oxide Fuel Cells (Sofcs), SSRN Electron. J. 923 (2022) 166351. https://doi.org/10.2139/ssrn.4076514.
[36] S.M. Mohamed, M.M.M. Sanad, Structural , Microstructural and Electrochemical Studies of Co / Mn Derived Oxides as Protective Layers for Intermediate Temperature SOFCs, 835 (2020) 353–358. https://doi.org/10.4028/www.scientific.net/KEM.835.353.

[37] P. Wei, M. Bieringer, L.M.D. Cranswick, A. Petric, In situ high-temperature X-ray and neutron diffraction of Cu-Mn oxide phases, J. Mater. Sci. 45 (2010) 1056–1064. https://doi.org/10.1007/s10853-009-4042-2.
[38] Y. Wang, Structure and Electrical Conductivity of Mn-based Spinels Used as Solid Oxide Fuel Cell Interconnect Coatings, McMaster University, Hamilton, Ontario, 2013.
[39] J. Ignaczak, Y. Naumovich, K. Górnicka, J. Jamroz, W. Wróbel, J. Karczewski, M. Chen, P. Jasiński, S. Molin, Preparation and characterisation of iron substituted Mn1.7Cu1.3-xFexO4 spinel oxides (x = 0, 0.1, 0.3, 0.5), J. Eur. Ceram. Soc. 40 (2020) 5920–5929. https://doi.org/10.1016/j.jeurceramsoc.2020.07.001.
[40] Z. Sun, S. Gopalan, U.B. Pal, S.N. Basu, Cu1.3Mn1.7O4 spinel coatings deposited by electrophoretic deposition on Crofer 22 APU substrates for solid oxide fuel cell applications, Surf. Coatings Technol. 323 (2017) 49–57. https://doi.org/10.1016/j.surfcoat.2016.09.028.
[41] R. Wang, Z. Sun, U.B. Pal, S. Gopalan, S.N. Basu, Mitigation of chromium poisoning of cathodes in solid oxide fuel cells employing CuMn1.8O4 spinel coating on metallic interconnect, J. Power Sources. 376 (2018) 100–110. https://doi.org/10.1016/j.jpowsour.2017.11.069.
[42] M. Bobruk, K. Brylewska, K. Durczak, K. Wojciechowski, A. Adamczyk, T. Brylewski, Synthesis of manganese-cobalt spinel via wet chemistry methods and its properties, Ceram. Int. 43 (2017) 15597–15609. https://doi.org/10.1016/j.ceramint.2017.08.116.
[43] B. Saravanakumar, S. Muthu Lakshmi, G. Ravi, V. Ganesh, A. Sakunthala, R. Yuvakkumar, Electrochemical properties of rice-like copper manganese oxide (CuMn2O4) nanoparticles for pseudocapacitor applications, J. Alloys Compd. 723 (2017) 115–122. https://doi.org/10.1016/j.jallcom.2017.06.249.
[44] M. Enhessari, A. Salehabadi, K. Maarofian, S. Khanahmadzadeh, Synthesis and Physicochemical Properties of CuMn2O4 Nanoparticles; a Potential Semiconductor for Photoelectric Devices, Int. J. Bio-Inorganic Hybrid Nanomater. 5 (2016) 115–120. https://www.researchgate.net/profile/Morteza_Enhessari/publication/311912768_Synthesis_and_physicochemical_properties_of_CuMn2O4_nanoparticles_a_potential_semiconductor_for_photoelectric_devices/links/5862259108ae8fce49085efd/Synthesis-and-physicochemical.
[45] Z. Lei, M. Shen, J. Jing, Z. Yang, S. Peng, Flexible Cu1.5Mn1.5O4 combined with Co3O4 and Al2O3 conductive ceramic film as a cathode current collecting layer for solid oxide fuel cells, J. Power Sources. 490 (2021) 229566. https://doi.org/10.1016/j.jpowsour.2021.229566.
[46] W. Huang, S. Gopalan, U.B. Pal, S.N. Basu, Evaluation of Electrophoretically Deposited CuMn[sub 1.8]O[sub 4] Spinel Coatings on Crofer 22 APU for Solid Oxide Fuel Cell Interconnects, J. Electrochem. Soc. 155 (2008) B1161. https://doi.org/10.1149/1.2975367.
[47] M. Bobruk, K. Durczak, J. Dąbek, T. Brylewski, Structure and Electrical Properties of Mn-Cu-O Spinels, J. Mater. Eng. Perform. 26 (2017) 1598–1604. https://doi.org/10.1007/s11665-017-2588-8.
[48] S.J. Cho, M.J. Uddin, P. Alaboina, Review of Nanotechnology for Cathode Materials in Batteries, Elsevier Inc., 2017. https://doi.org/10.1016/B978-0-323-42977-1.00003-0.
[49] Q.A. Pankhurst, R.J. Pollard, Structural and magnetic properties of ferrihydrite, Clays Clay Miner. 40 (1992) 268–272. https://doi.org/10.1346/CCMN.1992.0400303.
[50] S. Joshi, A. Petric, Nickel substituted CuMn2O4 spinel coatings for solid oxide fuel cell interconnects, Int. J. Hydrogen Energy. 42 (2017) 5584–5589. https://doi.org/10.1016/j.ijhydene.2016.08.075.

[51] Z. Sun, S. Gopalan, U.B. Pal, S.N. Basu, Electrophoretically Deposited Copper Manganese Spinel Coatings for Prevention of Chromium Poisoning in Solid Oxide Fuel Cells, Miner. Met. Mater. Ser. (2019) 265–272. https://doi.org/10.1007/978-3-030-06209-5_27.
[52] P.D. Kit, Material Data Sheet, (2001) 7072.
[53] R. Landauer, Electrical conductivity in inhomogeneous media, 2 (2008) 2–45. https://doi.org/10.1063/1.31150.
[54] A. Kruk, M. Mrózek, J. Domagała, T. Brylewski, W. Gawlik, Synthesis and physicochemical properties of yttrium oxide doped with neodymium and lanthanum, J. Electron. Mater. 43 (2014) 3611–3617. https://doi.org/10.1007/s11664-014-3250-y.
[55] H.A. Jahn, E. Teller, H.A. Jahn E. Teller, Stability of polyatomic molecules in degenerate electronic states - I—orbital degeneracy, Proc. R. Soc. London. Ser. A. 16 (1937) 220–235.
[56] J. Dunitz, L. Orgel, Electronic properties of transition-metal oxides—I: Distortions from cubic symmetry, J. Phys. Chem. Solids. 3 (1957) 20–29.
[57] J. Preudhomme, P. Tarte, Infrared studies of spinels-III. The normal II-III spinels, Spectrochim. Acta Part A Mol. Spectrosc. 27 (1971) 1817–1835. https://doi.org/10.1016/0584-8539(71)80235-0.
[58] D. Basak, J. Ghose, Infrared studies on some substituted copper chromite spinels, Spectrochim. Acta Part A Mol. Spectrosc. 50 (1994) 713–718. https://doi.org/10.1016/0584-8539(94)80008-1.
[59] B. Gillot, S. Buguet, E. Kester, Oxidation mechanism and valence states of copper and manganese in tetragonal CuMn2O4, J. Mater. Chem. 7 (1997) 2513–2517. https://doi.org/10.1039/a703731g.
[60] J. Vince, A. Šurca Vuk, U. Opara Krašovec, B. Orel, M. Köhl, M. Heck, Solar absorber coatings based on CoCuMnOx spinels prepared via the sol-gel process: Structural and optical properties, Sol. Energy Mater. Sol. Cells. 79 (2003) 313–330. https://doi.org/10.1016/S0927-0248(02)00457-9.
[61] A. Li, Y. Liu, Z. Wang, Z. Song, Y. Zhang, Y. Wang, B. Xu, F. Qi, A. Ikhlaq, J. Kumirska, E. Maria Siedlecka, Catalytic ozonation membrane reactor integrated with CuMn2O4/rGO for degradation emerging UV absorbers (BP-4) and fouling in-situ self-cleaning, Sep. Purif. Technol. 279 (2021). https://doi.org/10.1016/j.seppur.2021.119804.
[62] Tuning of eg electron occupancy of MnCo2O4 spinel for oxygen evolution reaction by partial substitution of Co by Fe at octahedral sites, Int. J. Hydrogen Energy. (2023).
[63] Y. Sun, H. Liao, J. Wang, B. Chen, S. Sun, S.J.H. Ong, S. Xi, C. Diao, Y. Du, J.O. Wang, M.B.H. Breese, S. Li, H. Zhang, Z.J. Xu, Covalency competition dominates the water oxidation structure–activity relationship on spinel oxides, Nat. Catal. 3 (2020) 554–563. https://doi.org/10.1038/s41929-020-0465-6.
[64] C.M. Julien, M. Massot, C. Poinsignon, Lattice vibrations of manganese oxides: Part I. Periodic structures, Spectrochim. Acta - Part A Mol. Biomol. Spectrosc. 60 (2004) 689–700. https://doi.org/10.1016/S1386-1425(03)00279-8.
[65] S.J. Parikh, J. Chorover, FTIR spectroscopic study of biogenic Mn-oxide formation by Pseudomonas putida GB-1, Geomicrobiol. J. 22 (2005) 207–218. https://doi.org/10.1080/01490450590947724.
[66] A. Rita, A. Sivakumar, S.A. Martin Britto Dhas, Influence of shock waves on structural and morphological properties of copper oxide NPs for aerospace applications, J. Nanostructure Chem. 9 (2019) 225–230. https://doi.org/10.1007/s40097-019-00313-0.
[67] V. Sudha, G. Murugadoss, R. Thangamuthu, Structural and morphological tuning of Cu-based metal oxide nanoparticles by a facile chemical method and highly

electrochemical sensing of sulphite, Sci. Rep. 11 (2021) 1–12. https://doi.org/10.1038/s41598-021-82741-z.
[68] J. Han, J. Chang, R. Wei, X. Ning, J. Li, Z. Li, H. Guo, Y. Yang, Mechanistic investigation on tuning the conductivity type of cuprous oxide (Cu2O) thin films via deposition potential, Int. J. Hydrogen Energy. 43 (2018) 13764–13777. https://doi.org/10.1016/j.ijhydene.2018.02.121.
[69] Y. Wang, Y. Lü, W. Zhan, Z. Xie, Q. Kuang, L. Zheng, Synthesis of porous Cu2O/CuO cages using Cu-based metal-organic frameworks as templates and their gas-sensing properties, J. Mater. Chem. A. 3 (2015) 12796–12803. https://doi.org/10.1039/c5ta01108f.
[70] M. Swadźba-Kwaśny, L. Chancelier, S. Ng, H.G. Manyar, C. Hardacre, P. Nockemann, Facile in situ synthesis of nanofluids based on ionic liquids and copper oxide clusters and nanoparticles, Dalt. Trans. 41 (2012) 219–227. https://doi.org/10.1039/c1dt11578b.
[71] P.R. Ilango, K. Prasanna, S.J. Do, Y.N. Jo, C.W. Lee, Eco-friendly nitrogen-containing carbon encapsulated LiMn2O4 cathodes to enhance the electrochemical properties in rechargeable Li-ion batteries, Sci. Rep. 6 (2016) 2–10. https://doi.org/10.1038/srep29826.
[72] M. Wang, K. Chen, J. Liu, Q. He, G. Li, F. Li, Efficiently enhancing electrocatalytic activity of α-MnO2 nanorods/N-doped ketjenblack carbon for oxygen reduction reaction and oxygen evolution reaction using facile regulated hydrothermal treatment, Catalysts. 8 (2018). https://doi.org/10.3390/catal8040138.
[73] P. Kupracz, A. Lenarciak, M. Łapiński, M. Prześniak-Welenc, N.A. Wójcik, R.J. Barczyński, Polaron hopping conduction in manganese borosilicate glass, J. Non. Cryst. Solids. 458 (2017) 15–21. https://doi.org/10.1016/j.jnoncrysol.2016.12.008.
[74] K. Cysewska, M. Zając, M. Łapiński, J. Karczewski, M.K. Rybarczyk, B. Kamecki, P. Jasiński, S. Molin, The Effect of Cobalt Incorporation into Nickel–Iron Oxide/(oxy)hydroxide Catalyst on Electrocatalytic Performance Toward Oxygen Evolution Reaction, Energy Technol. 9 (2021). https://doi.org/10.1002/ente.202100688.
[75] M. Rosenberg, P. Nicolau, R. Manaila, P. Pausescu, Preparation, electrical conductivity and tetragonal distortion of some manganite-systems, J. Phys. Chem. Solids. 24 (1963) 1419–1434. https://doi.org/10.1016/0022-3697(63)90083-0.
[76] S.E. DORRIS, T.O. MASON, Electrical Properties and Cation Valencies in Mn3O4, J. Am. Ceram. Soc. 71 (1988) 379–385. https://doi.org/10.1111/j.1151-2916.1988.tb05057.x.
[77] P. Stallinga, Electronic transport in organic materials: Comparison of band theory with percolation/(variable range) hopping theory, Adv. Mater. 23 (2011) 3356–3362. https://doi.org/10.1002/adma.201101129.
[78] D. Lee, J.H. Han, Y. Chun, R.H. Song, D.R. Shin, Preparation and characterization of strontium and magnesium doped lanthanum gallates as the electrolyte for IT-SOFC, J. Power Sources. 166 (2007) 35–40. https://doi.org/10.1016/j.jpowsour.2006.12.099.
[79] S.H. Jo, P. Muralidharan, D.K. Kim, Electrical characterization of dense and porous nanocrystalline Gd-doped ceria electrolytes, Solid State Ionics. 178 (2008) 1990–1997. https://doi.org/10.1016/j.ssi.2007.12.076.
[80] I.G. Austin, N.F. Mott, Polarons in crystalline and non-crystalline materials, Adv. Phys. 50 (2001) 757–812. https://doi.org/10.1080/00018730110103249.
[81] T. Brylewski, A. Kruk, M. Bobruk, A. Adamczyk, J. Partyka, P. Rutkowski, Structure and electrical properties of Cu-doped Mn-Co-O spinel prepared via soft chemistry and its application in intermediate-temperature solid oxide fuel cell interconnects, J. Power Sources. 333 (2016) 145–155. https://doi.org/10.1016/j.jpowsour.2016.09.136.

[82] N. Ponpandian, P. Balaya, A. Narayanasamy, Electrical conductivity and dielectric behaviour of nanocrystalline NiFe2O4 spinel, J. Phys. Condens. Matter. 14 (2002) 3221–3237. https://doi.org/10.1088/0953-8984/14/12/311.
[83] A. Niemczyk, Z. Du, A. Olszewska, M. Marzec, M. Gajewska, K. Świerczek, H. Zhao, B. Poudel, B. Dabrowski, Effective oxygen reduction on A-site substituted LaCuO3-: δ: Toward air electrodes for SOFCs based on perovskite-type copper oxides, J. Mater. Chem. A. 7 (2019) 27403–27416. https://doi.org/10.1039/c9ta09244g.
[84] Z. Sun, R. Wang, A.Y. Nikiforov, S. Gopalan, U.B. Pal, S.N. Basu, CuMn1.8O4 protective coatings on metallic interconnects for prevention of Cr-poisoning in solid oxide fuel cells, J. Power Sources. 378 (2018) 125–133. https://doi.org/10.1016/j.jpowsour.2017.12.031.
[85] N. Hosseini, M.H. Abbasi, F. Karimzadeh, G.M. Choi, Development of Cu1.3Mn1.7O4 spinel coating on ferritic stainless steel for solid oxide fuel cell interconnects, J. Power Sources. 273 (2015) 1073–1083. https://doi.org/10.1016/j.jpowsour.2014.10.017.
[86] A. Norouzi, M. Soltanieh, S. Rastegari, An electrophoretic co-deposition of metal oxides followed by in-situ copper manganese spinel synthesis on AISI-430 for application in SOFC interconnects, Int. J. Hydrogen Energy. 47 (2022) 14346–14360. https://doi.org/10.1016/j.ijhydene.2022.02.182.